# Enforcement of interface laws for dissipative vibro-acoustic problems within high-order X-FEM

Shaoqi Wu, Grégory Legrain, Olivier Dazel

# Enforcement of interface laws for dissipative vibro-acoustic problems within high-order X-FEM

Shaoqi Wu[a], Grégory Legrain[a] and Olivier Dazel[b]

[a] Nantes Université, École Centrale Nantes, CNRS, GeM, UMR 6183, F-44000 Nantes, France
[b] Le Mans Université, CNRS UMR CNRS 6613, 72085 Le Mans Cedex, France

This work elaborates on the numerical solution to cope with the enforcement of a general robin-type weak/strong discontinuity interface in acoustic problems, where energy dissipative media with complex-valued properties are involved. We propose a discrete variational formulation based on the idea of Nitsche's method in the eXtended Finite Element Method (X-FEM) framework. The formulation is stable in the sense that it is able to treat any interface parameters accurately within any mesh configuration and approximation order. We prove the stability of the method, fully considering the effects of energy dissipation, and provide a robust strategy involving basis conversion to obtain the stability parameter. Numerical examples demonstrate that the proposed discrete formulation gives an optimal solution in terms of accuracy and conditioning, compared to a penalty-like formulation. For all interface types, optimal rates of convergence are achieved on both primal and dual variables. Our method exhibits high robustness and stability regardless of discretization, geometries, materials, excitation frequency and interface parameters.

*Interface laws; Dissipative acoustic; Nitsche's formulation; high-order X-FEM*

## 1. Introduction

Thin layers are widely used in vibro-acoustic systems such as sound proofing, imperious screen and porous films. They are usually employed in conjunction with bulk sound dissipation materials to constitute sound attenuation systems. One can find such systems

extensively in the automotive/aircraft industry on the wind front windows or as passive noise reduction components coated on cabin seats. This paper focuses on simulating sound propagation in systems that comprise both thick and thin dissipative layers. As one of the frequently used sound dissipation materials, porous materials present a high performance in absorbing vibration energy resulting from an intrinsic interaction between saturated air and elastic frame. Concerning the physical models for such acoustic materials, Biot's theory [1, 2] provides two fully coupled equations linking the homogenized solid and fluid phases, where the propagation of solid and pressure waves are simultaneously considered. Equivalent fluid models such as the JCA (Johnson-Champoux-Allard) [3, 4] and Limp models [5] were also developed as an alternative to the Biot theory, assuming that the frame is motionless and that the energy dissipation is accounted for by complex-valued material parameters. This class of models will be considered in this contribution. As the thickness of the thin acoustic layers is relatively small compared to the size of the entire system, one usually reduces it to a null-thickness interface with an appropriate interface condition [6]. In particular, the pressure drop model [7] is considered in the current work.

The numerical solution of such acoustic problems using spatial discretization methods, could be computationally demanding. In particular, time-harmonic Helmholtz equations are known to suffer from dispersion error [8] in large-scale domains or when subjected to high frequency excitations, for which high-resolution meshes [9], high order [10, 11, 12] or wave-based [13] approximations are necessary. In addition, conventional mesh-based numerical methods require geometrically conforming meshes where the boundaries of the elements have to align with the geometries. This leads to more complicated and time-costly pre-processing steps when the boundaries of the interfaces are complex or when dealing with interfaces subjected to topological variations. In order to alleviate these numerical restrictions seamlessly, high-order approximation methods combined with techniques that are able to handle unfitted meshes are appealing. Within these techniques, the approximation of the solution and the geometry can be treated independently. However, the enforcement of potentially discontinuous interface conditions inside elements and the representation of complex geometries with high-order approximations need to be appropriately addressed.

One major family of the relevant methods is the eXtended Finite Element Method (X-FEM). This method may first trace back to the work of Moës et al.[14], where the concept of the X-FEM was proposed to address crack propagation problems without *re-meshing*. The X-FEM is considered as a special case of the Generalized Finite Element Method (GFEM [15]) where the whole or a part of the computational domain is *enriched* by additional functions to represent complex features of the solution such as discontinuities, singularities or other non-smooth behaviours. With the versatility of the enrichment, in the past two decades, the X-FEM has been applied extensively to model holes [16], inclusions [16, 17] and phases interfaces [18], etc. (for more applications, see [19]). Heaviside enriched X-FEM has even become one of the most widely used numerical methods to treat fracture problems [20]. Meanwhile, Hansbo and Hansbo [21] proposed an unfitted finite element method to treat discontinuities across interfaces. Instead of using an enrichment, two *overlapping* elements are defined over the interface through

the concept of phantom [22] or ghost [23] nodes. This setup allows the construction of a discontinuous approximation basis to model the discontinuity. This method, which has been applied, from solid mechanics [24], fluid-structure interaction [25] to stokes interface [26] and many other problems [27, 28], is now being well-known as the family of Cut-FEM methods (see review [29]). Although the Cut-FEM can be seen as a reparametrization of the Heaviside enriched X-FEM, spanning the same approximation space [30], the resulting algebraic systems (matrices) are not identical. The effect of this aspect during the computation is rarely recognized in former studies, which will be clarified as well in this work.

Properly prescribing the boundary/interface conditions within the aforementioned methods might be a key ingredient. The penalty method [31] could be the most straightforward candidate to impose Dirichlet boundary conditions or enforce the continuity of the solution at the interfaces. However, it is not consistent with the original problems, and it requires a sufficiently large penalty parameter to retain an optimal convergence rate, which eventually destroys the conditioning of the discrete system. Another classical approach to weakly prescribe the boundary conditions is Lagrange multipliers [18]. Within this approach, the multiplier space needs to be chosen carefully to satisfy the well-known inf-sup or LBB stability condition [32]. Moreover, this method further increases the number of degrees of freedom. In order to address these issues, Nitsche's variational approach [33] or augmented Lagrange multipliers [34] were proposed, replacing the Lagrangian multiplier by a representation of the boundary flux together with a penalty term for stabilization. In the context of unfitted-FEM methods, this approach was first introduced in [21] for elliptic interface problems and then was applied for non-matching meshes [25], fictitious domain [35, 36] and embedded interfaces [37, 38]. Nitsche's method has become a standard ingredient when using the Cut-FEM approach. Furthermore, Ghost penalty [39, 40] and $\gamma$-Nitsche [41, 42, 43] were also proposed to improve the stability of Nitsche's formulation in the context of cut elements.

Regarding the numerical solution of the Helmholtz equation using Nitsche's method, we revisit the two most relevant former works. One of them was conducted by Zou et al. [23], where Nitsche's formulation is applied for a classical two-media steady-state acoustic problem, where a perfect interface (continuity of the pressure field) was enforced. The problem was solved using a linear Cut-FEM approach. The second work was carried out by Yedeg et al.[44], and discussed a Nitsche-type formulation for a complex-valued transmission interface condition. This formulation is especially attractive because the two extreme cases (perfect and imperfect interfaces) can be recovered by a unique formulation. In their work, a single homogeneous media was involved, and a conforming finite element mesh was required to discretize the computational domain. From a physical point of view, our problem of interest includes multiple different complex-valued dissipative media that have not yet been investigated for strong/weak discontinuity interface problems. From a numerical point of view, our solution will be approximated using a high-order Heaviside enriched X-FEM space that is different from any discretization space analyzed in the literature.

The work presented in this paper enlarges the application of high-order X-FEM and Nitsche's method to acoustic dissipative problems. The main contributions are as follows:

Firstly, based on the idea proposed in [24, 44], we discuss the effect of complex-valued media and robin-type interface condition involved in a Nitsche-type formulation. The proof of stability and the lower bound of its parameter are provided. Secondly, we elaborate on the equivalence and difference between the Heaviside enriched X-FEM and Cut-FEM for our problem of interest, in particular the influence on the estimation of the stability parameter. Finally, we verify numerically the critical choice of stabilization and highlight the stability and robustness of the proposed Nitsche-type formulation with respect to interface laws, and compare it with the penalty-like method.

The rest of the paper is organized as follows: In section 2, the problem of interest is stated with corresponding strong and weak formulations. Section 3 is dedicated to the discussion on discretization, including the emphasis on the difference between X-FEM and Cut-FEM basis in our case, in addition to the proof of coercivity for the discrete formulation. Two strategies to compute the stability parameters in the current framework are presented as well in this section. In section 4, the proposed method is assessed against a series of numerical examples with gradual geometrical complexity to verify the theoretical proofs and implementation. Several significant numerical conclusions are reported. At last, section 5 gives concluding remarks and perspectives to our work.

# 2. Problem statement and formulation

## 2.1. Model and strong form

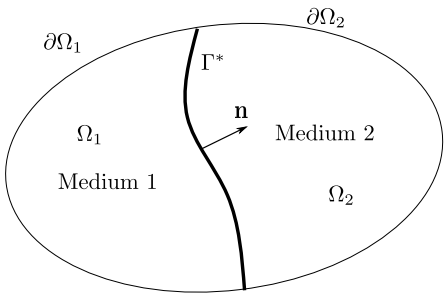


Figure 1: Two-media sound propagation configuration

For the sake of simplicity, we confine attention to a two-dimensional two-media domain $\Omega \in \mathbb{R}^2$ as illustrated in fig. 1, partitioned into subdomain $\Omega_1$ and $\Omega_2$ with $\Omega_1 \cup \Omega_2 = \Omega$, $\Omega_1 \cap \Omega_2 = \emptyset$. The subdomains represent bulk acoustic media such as air and energy dissipative material, respectively. The domain is enclosed by the boundary $\partial\Omega_1 \cup \partial\Omega_2 = \partial\Omega$ associated with the corresponding subdomains. We suppose that a thin layer exists between the two media, such as a resistive sound film, which is reduced to a null-thickness interface $\Gamma^*$ with an outward normal $\mathbf{n}$ pointing from $\Omega_1$ to $\Omega_2$. It is noted that this outward unit normal $\mathbf{n}$ is not only needed on the interface, but is also used to define the Neumann boundary conditions presented in eq. (4). The terms related to such normal need to be treated carefully in order to obtain correct signs in the final formulations.

As mentioned before, this paper considers dissipative materials as equivalent fluids. Sound propagation in such media is hence described by the classical Helmholtz equation (which, in the case of air, involves only real-valued parameters). Thus, the governing equations under the time dependence $e^{+\mathrm{j}\omega t}$ with angular frequency $\omega$ for both bulk parts are written in the following way:

$$\nabla^2 p_i + k_i^2 p = 0, \quad i = 1, 2, \tag{1}$$

where $p_i$ corresponds to the acoustic pressure in each subdomain, and $\nabla^2\bullet$ represents the Laplacian operator. Coefficient $k_i$ denotes the wave number of the medium that is defined as $k_i = \omega/c_i$ where $c_i$ is the sound velocity in the medium. The wave number is a complex number when modelling energy dissipative materials.

At the interface, an interface law is enforced to model the thin acoustic resistive layers. These layers induce a pressure difference due to their flow resistivity $\sigma$ [7, 45], so-called pressure jump model. In addition, flow velocity is assumed to be conserved at the interface $\Gamma^*$ as the thickness of the resistive layer is small compared to the characteristic length of the whole computational domain. Then, the interface conditions are expressed as:

$$p_1 - p_2 = \sigma d \bar{v} \quad \text{on}\, \Gamma^*, \tag{2a}$$

$$\frac{1}{\rho_1}\frac{\partial p_1}{\partial n} = \frac{1}{\rho_2}\frac{\partial p_2}{\partial n} \quad \text{on}\, \Gamma^*, \tag{2b}$$

in which $d$ denotes the thickness of the thin layer and $\rho_i$ are effective fluid densities (complex-valued for dissipative media). $\bar{v}$ represents the mean flow velocity at the interface, which is defined as:

$$\bar{v} = -\frac{1}{\mathrm{j}\omega\rho_1}\frac{\partial p_1}{\partial n} = -\frac{1}{\mathrm{j}\omega\rho_2}\frac{\partial p_2}{\partial n} \quad \text{on}\, \Gamma^*, \tag{3}$$

where the two expressions in eq. (3) are identical due to the continuity condition eq. (2b). However, when the problem is solved numerically by means of the finite element method, the mean flow velocity is related to the numerical solution of interfacial flux (normal gradient), which will depend on the discretization as well. In that case, the definition of this flow quantity becomes more crucial, which will be addressed in the following section.

Combing the bulk governing equations eq. (1) for the two media and the interface conditions given in eq. (2), the description of the boundary value problem (BVP) written on the whole domain equipped with Neumann boundary conditions on $\partial\Omega_i$ reads as:

$$\sum_{i=1}^{2} \left(\nabla^2 p + k_i^2 p\right) = 0 \quad \text{in}\, \Omega_1 \cup \Omega_2, \tag{4a}$$

$$\frac{\partial p}{\partial n} = g_N \quad \text{on}\, \partial\Omega_1 \cup \partial\Omega_2, \tag{4b}$$

$$[\![p]\!] - \sigma d \bar{v} = 0 \quad \text{on}\, \Gamma^*, \tag{4c}$$

$$[\![\frac{1}{\rho}\frac{\partial p}{\partial n}]\!] = 0 \quad \text{on}\, \Gamma^*, \tag{4d}$$

where $[\![\bullet]\!]$ is the jump operator $[\![\bullet]\!] = \bullet_1 - \bullet_2$ at the interface $\Gamma^*$. $g_N$ is the known value of the Neumann boundary condition. It is worth emphasizing that the pressure discontinuity eq. (4c) depends on the change of its gradient, which corresponds to a generalized Robin interface condition. For the particular situation, where $\sigma d = 0$, the pressure will be continuous at the interface, and the interface will be said "perfect" in the following.

Remark that the existence and uniqueness of the solution for the above problem equipped with Neumann boundary conditions and energy damping (could be dissipative media and/or pressure jump) has already been discussed in [46], so that it will not be presented here in detail.

## 2.2. Penalty-type weak formulation

In general, the weak solution to the prescribed problem could be formulated as a variational form as follows: find $p \in \mathcal{P} = H^1(\Omega_1 \cup \Omega_2)$ such that

$$a(q,p) = \ell(q) \quad \forall q \in H^1(\Omega_1 \cup \Omega_2), \tag{5}$$

where the right-hand linear form $\ell(q)$ originates from the Neumann boundary conditions. In our case, the bilinear form consists of two parts: the first one denoted as $a_B$ from the two bulk subdomains $\Omega_1$ and $\Omega_2$ and the second one denoted $a_I$ defined on the interface $\Gamma^*$ as follows:

$$a(q,p) := a_B(q,p) + a_I(q,p). \tag{6}$$

The key point for this bilinear form is to impose two interface conditions on $\Gamma^*$. Conservation of velocity eq. (4d) is directly satisfied when multiplying the bulk governing equations by $1/\rho_i$. With the test function $q \in \mathcal{P}$ as well, $a_B$ is rewritten as:

$$a_B(q,p) := \sum_i^2 \left( \int_{\Omega_i} \frac{1}{\rho_i} \boldsymbol{\nabla} q \boldsymbol{\nabla} p \, \mathrm{d}\Omega - \int_{\Omega_i} \frac{\omega^2}{K_i} q p \, \mathrm{d}\Omega \right), \tag{7}$$

where $k_i^2/\rho_i$ is modified to $k = \omega/c_i$ and bulk compressibility $K_i = \rho_i c_i^2$ (this modification aims at facilitating the following stability analysis). Regarding the interface integrals on $\Gamma^*$, we have:

$$a_I(q,p) := -\int_{\Gamma^*} \frac{q_1}{\rho_1} \frac{\partial p_1}{\partial n} \mathrm{d}S + \int_{\Gamma^*} \frac{q_2}{\rho_2} \frac{\partial p_2}{\partial n} \mathrm{d}S, \tag{8}$$

thanks to the conservation of the mean velocity eq. (3), $a_I$ can be written as:

$$a_I(q,p) = \int_{\Gamma^*} \mathrm{j}\omega \bar{v} [\![q]\!] \mathrm{d}S, \tag{9}$$

then, with the pressure jump condition eq. (4c), $\bar{v}$ is replaced, and the final interface bilinear form is obtained:

$$a_I(q,p) = \frac{\mathrm{j}\omega}{\sigma d} \int_{\Gamma^*} [\![q]\!] [\![p]\!] \mathrm{d}S. \tag{10}$$

This interface term is similar to spring-like interfaces in solid mechanics, as studied in [47] or is called "substitution" method as in [28]. This term has a similar form to the penalty method [31] to enforce the Dirichlet boundary condition but with real physical constants $\sigma$, $d$ and $\omega$ instead of a pure numerical parameter in the case of penalization. This means that once the physical problem is determined, the weak formulation can be readily implemented and solved directly without additional numerical terms. Moreover, in contrast to conventional penalty methods, such penalty-type formulation is variationally consistent with the original problem, and the interface pressure jump condition is preserved naturally. This type of formulation has been shown to lead to good performances within the X-FEM in [48] to treat composite materials. For the following analysis, the results of the *penalty-type* formulation are regarded as a reference.

However, this formulation is not able to model a perfect interface and also cases where $\sigma d \to 0$ for which the corresponding linear system could be potentially ill-conditioned, especially when using X-FEM method. Therefore, we strive to derive a more general and stable variational formulation in the sense that it can treat seamlessly perfect and imperfect interfaces, while preserving the conditioning of the discrete system regardless of the physical parameters of the interface law.

## 2.3. Nitsche-type weak formulation

We derive a Nitsche-type formulation relied on the idea proposed in [47, 44]. To this end, we first rewrite the mean flow velocity at the interface as:

$$\bar{v} := -\frac{1}{\mathrm{j}\omega}\left(\frac{\gamma_1}{\rho_1}\frac{\partial p_1}{\partial n} + \frac{\gamma_2}{\rho_2}\frac{\partial p_2}{\partial n}\right) = -\frac{1}{\mathrm{j}\omega}\left\langle \frac{1}{\rho}\frac{\partial p}{\partial n}\right\rangle_\gamma, \tag{11}$$

in which, $\langle \bullet \rangle_\gamma$ refers to the weighted-average operator with $\gamma_1 + \gamma_2 = 1$. As aforementioned, in the continuous case, any admissible $\gamma_i$ could be chosen leading to a same resulting mean flow since the continuity of the velocity at the interface is always guaranteed. The choice of the weighting parameter has a non-negligible influence on the numerical solution, especially here when interface embedded methods such as the X-FEM are employed. A detailed discussion for choosing a suitable $\gamma$ will be stated in section 3.

With such mean flow expression, the pressure jump condition eq. (2a) is rewritten as:

$$[\![p]\!] + \frac{\sigma d}{\mathrm{j}\omega}\left\langle \frac{1}{\rho}\frac{\partial p}{\partial n}\right\rangle_\gamma = 0. \tag{12}$$

Thus, the interface term $a_I$ in eq. (8) becomes:

$$a_I^*(q,p) = -\int_{\Gamma^*} [\![q]\!] \left\langle \frac{1}{\rho}\frac{\partial p}{\partial n}\right\rangle_\gamma \mathrm{d}S. \tag{13}$$

Following by addition and subtraction of $\frac{\sigma d}{\mathrm{j}\omega}\left\langle \frac{1}{\rho}\frac{\partial q}{\partial n}\right\rangle_\gamma \left\langle \frac{1}{\rho}\frac{\partial p}{\partial n}\right\rangle_\gamma$, we obtain:

$$a_I^*(q,p) = -\int_{\Gamma^*}\left\langle \frac{1}{\rho}\frac{\partial p}{\partial n}\right\rangle_\gamma \left(\llbracket q\rrbracket + \frac{\sigma d}{j\omega}\left\langle \frac{1}{\rho}\frac{\partial q}{\partial n}\right\rangle_\gamma\right)\mathrm{d}S + \int_{\Gamma^*}\frac{\sigma d}{j\omega}\left\langle \frac{1}{\rho}\frac{\partial q}{\partial n}\right\rangle_\gamma \left\langle \frac{1}{\rho}\frac{\partial p}{\partial n}\right\rangle_\gamma \mathrm{d}S, \tag{14}$$

then, we symmetrize the formulation with the interface condition eq. (12):

$$\begin{aligned} a_I^*(q,p) := &-\int_{\Gamma^*}\left\langle \frac{1}{\rho}\frac{\partial p}{\partial n}\right\rangle_\gamma \left(\llbracket q\rrbracket + \frac{\sigma d}{j\omega}\left\langle \frac{1}{\rho}\frac{\partial q}{\partial n}\right\rangle_\gamma\right)\mathrm{d}S - \int_{\Gamma^*}\left\langle \frac{1}{\rho}\frac{\partial q}{\partial n}\right\rangle_\gamma \left(\llbracket p\rrbracket + \frac{\sigma d}{j\omega}\left\langle \frac{1}{\rho}\frac{\partial p}{\partial n}\right\rangle_\gamma\right)\mathrm{d}S \\ &+ \int_{\Gamma^*}\frac{\sigma d}{j\omega}\left\langle \frac{1}{\rho}\frac{\partial q}{\partial n}\right\rangle_\gamma \left\langle \frac{1}{\rho}\frac{\partial p}{\partial n}\right\rangle_\gamma \mathrm{d}S, \end{aligned} \tag{15}$$

finally, the formulation is stabilized by a term weighted by a coefficient $\lambda$ to be defined:

$$\begin{aligned} a_I^*(q,p) := &\underbrace{-\int_{\Gamma^*}\left\langle \frac{1}{\rho}\frac{\partial p}{\partial n}\right\rangle_\gamma \left(\llbracket q\rrbracket + \frac{\sigma d}{\mathrm{j}\omega}\left\langle \frac{1}{\rho}\frac{\partial q}{\partial n}\right\rangle_\gamma\right)\mathrm{d}S}_{\text{consistency}} \underbrace{-\int_{\Gamma^*}\left\langle \frac{1}{\rho}\frac{\partial q}{\partial n}\right\rangle_\gamma \left(\llbracket p\rrbracket + \frac{\sigma d}{\mathrm{j}\omega}\left\langle \frac{1}{\rho}\frac{\partial p}{\partial n}\right\rangle_\gamma\right)\mathrm{d}S}_{\text{symmetry}} \\ &+ \int_{\Gamma^*}\frac{\sigma d}{\mathrm{j}\omega}\left\langle \frac{1}{\rho}\frac{\partial q}{\partial n}\right\rangle_\gamma \left\langle \frac{1}{\rho}\frac{\partial p}{\partial n}\right\rangle_\gamma \mathrm{d}S + \underbrace{\lambda\int_{\Gamma^*}\left(\llbracket q\rrbracket + \frac{\sigma d}{\mathrm{j}\omega}\left\langle \frac{1}{\rho}\frac{\partial q}{\partial n}\right\rangle_\gamma\right)\left(\llbracket p\rrbracket + \frac{\sigma d}{\mathrm{j}\omega}\left\langle \frac{1}{\rho}\frac{\partial p}{\partial n}\right\rangle_\gamma\right)\mathrm{d}S}_{\text{stabilization}}. \end{aligned} \tag{16}$$

Therefore, the Nitsche-based bilinear form for the problem given in eq. (4) writes:

$$a_\lambda(q,p) := a_B(q,p) + a_I^*(q,p), \tag{17}$$

where the integral involving $\lambda$ ensures the stability (coercivity) of the formulation above. As seen that when $\sigma d = 0$, the bilinear form becomes the standard Nitsche's formulation that enforces the continuity at the interface as [23] with stability parameter $\lambda$. On the other hand, when choosing $\lambda = \mathrm{j}\omega/(\sigma d)$, this formulation is reduced to the *penalty-type* one eq. (10). In fact, with a clever expression of $\lambda$, the *Nitsche-type* formulation can be bounded between these two extreme cases to take advantage of both formulations, which will be presented lately.

# 3. Spatial discretization

## 3.1. Implicit interface and eXtended Finite Element Method (X-FEM)

In the general framework of unfitted-FEM, the interface or the boundary (see fictitious domain method [35]) are usually described implicitly by means of level-set functions [49]. For the considered two media problem we choose $\Omega \in \mathbb{R}^2$, and discretize the domain $\Omega = \Omega_1 \cup \Omega_2$ into a set of non-overlapping triangular elements $\Omega_e$, constituting a mesh. A discrete level-set function is obtained by interpolation on this mesh as:

$$\phi(\mathbf{x}) = \sum_{i}^{n} N_i(\mathbf{x})\phi_i, \tag{18}$$

where $N_i(\mathbf{x})$ represent the standard finite elements shape functions and $\phi_i$ are the signed distances from finite element nodes to the interface. The computational domain is classified with the help of the sign of the level-set function, and the interface $\Gamma^*$ is located as the iso-zero curve:

$$\Gamma^* = \{\mathbf{x} \in \mathbb{R}^2 : \phi(\mathbf{x}) = 0\}. \tag{19}$$

Note that a geometrical error will appear when a curved interface is described because of the linear approximation of the level-set. This will degrade the convergence rate if a high-order approximation is considered. To mitigate such numerical issue, the strategy proposed in [50] is adopted, where the mesh used to approximate the solution is decoupled from the one used to interpolate the level-set function. The interface is defined on an adaptively refined mesh, while the high order solution is still approximated on a coarse uniform mesh. Contrary to the standard interface-fitted FEM, our solution is approximated on an extended finite element space $\mathcal{P}_h^{XFE}$ ($\mathcal{P}_h$ in the following) enlarging the standard FE space with an enriched one such that:

$$\mathcal{P}_h^{XFE} = \mathcal{P}_h^{FE} \oplus \mathcal{P}_h^{ENR}, \tag{20}$$

where the enrichment space is only defined on the elements intersecting with the interface to introduce special features in the solution. According to the type of discontinuity to be modelled (crack, hole or material inclusion), there exists many enrichment strategies and enrichment functions[16, 17, 51]. In the considered problem, as a pressure jump (potential strong discontinuity) is introduced at the material interface, the pressure field is approximated by $p_h \in \mathcal{P}_h \in \mathcal{P}$, such that:

$$p_h(\mathbf{x})\Big|_{\Omega_e} = \sum_{i}^{n} N_i(\mathbf{x})p_i + \sum_{j}^{n_{enr}} N_j(\mathbf{x})H(\mathbf{x})a_{pj}, \tag{21}$$

with $H(\mathbf{x})$ denoting the generalized Heaviside function:

$$H(\mathbf{x}) = \begin{cases} 1 & \phi(\mathbf{x}) \geq 0 \\ -1 & \phi(\mathbf{x}) < 0, \end{cases} \tag{22}$$

where $N_i(\mathbf{x})$ and $N_j(\mathbf{x})$ are the shape functions associated to the standard and enriched degrees of freedom respectively. The later one could be different from the ones used for standard degrees of freedom but needs to satisfy the partition of unity [52] (thus they are usually taken to be the same as $N_i$). In this work, high order Bernstein shape functions will be used for the approximation. Coefficients $a_{pj}$ are the enriched degrees of freedoms used to represent the discontinuity. As mentioned that the enriched part is only defined on the elements containing interfaces, the number of enriched degrees freedoms remains small: $n_{enr} \ll n$.

Arising from such discretization, the computational domain includes standard elements, fully enriched elements and partially enriched elements also called blending elements as shown in fig. 2. As the material interface is allowed to be embedded in elements,

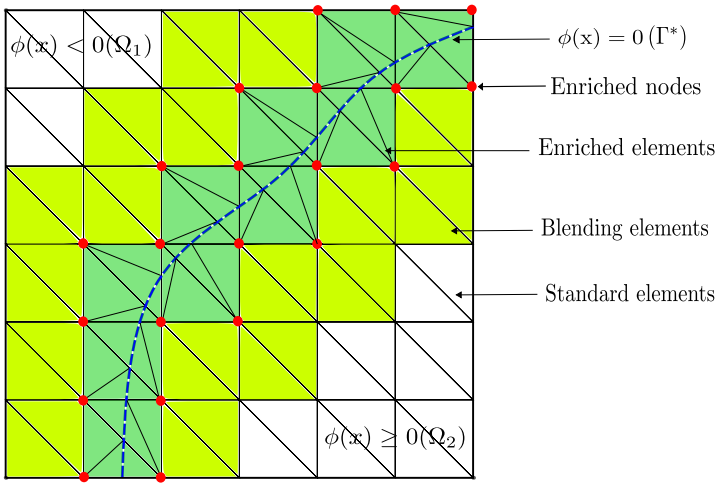


Figure 2: 2D domain cut by an interface: Standard, enriched and blending elements. Sub-triangulation is shown in the enriched elements.

one enriched element may contain multiple materials with different physical properties. The elements containing the interface are therefore partitioned into sub triangular elements to facilitate the association between an element (sub-element) and a material type, and to apply a modified Gauss quadrature for the weak formulation [16].

As mentioned in the section 1, the Heaviside-enriched X-FEM approximation eq. (21) is different from the one commonly used in the Cut-FEM community [21, 47, 37, 41, 38, 52, 26, 42, 23]. In fact, the latter one is usually being confused with X-FEM in the literature because of its similarity concerning the resulting approximation space as with X-FEM. The Cut-FEM is considered as an overlapping of standard finite elements [21] across the interface, which can be seen as the reparametrization of the Heaviside enriched X-FEM [30]. However, the structure of the resulting algebraic matrices are not identical. This distinction leads to different manipulations to calculate some element-wise quantities, such as the stability parameters for Nitsche's formulation, which will be thoroughly discussed in the section 3.3.

Here, we first address this difference by comparing the two bases in a 1D linear element for the convenience of illustration, as depicted in fig. 3. Functions $N_i^+$ and $N_i^-$ in fig. 3(b) represent the shape functions within Cut-FEM on each side of the interface, which are independent of the one to the other side. However, for X-FEM, it can be seen that the approximation on both sides involves all four shape functions. It is worth noting that this difference holds as well for higher order shape functions with the same numerical effects.

Despite this difference, the two basis can be linked by a simple relationship with

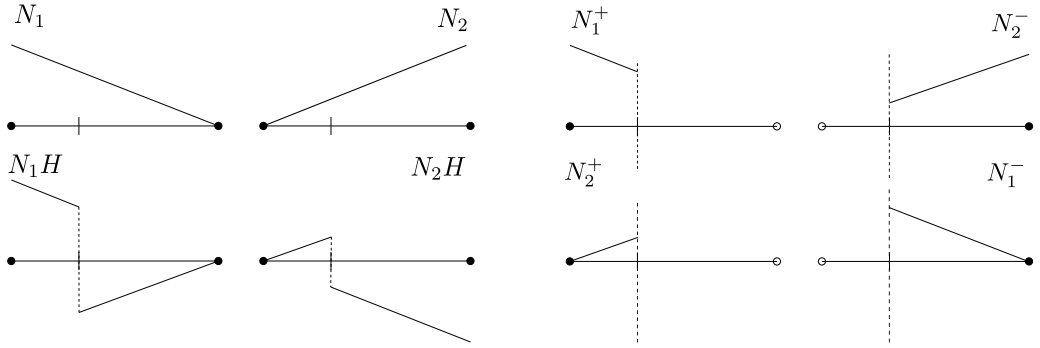


(a) Heaviside X-FEM (b) Hansbo Cut-FEM

Figure 3: 1D example of linear elements for (a) Heaviside X-FEM and (b) Hansbo's Cut-FEM for a strong discontinuity

following arrangement of degrees of freedom:

$$\begin{Bmatrix} N_1^+ \\ N_2^+ \\ N_1^- \\ N_2^- \end{Bmatrix} = \frac{1}{2} \begin{bmatrix} 1 & 0 & 1 & 0 \\ 0 & 1 & 0 & 1 \\ 1 & 0 & -1 & 0 \\ 0 & 1 & 0 & -1 \end{bmatrix} \begin{Bmatrix} N_1 \\ N_2 \\ N_1 H \\ N_2 H \end{Bmatrix}, \tag{23}$$

which can be readily extended to general higher order basis as:

$$\begin{Bmatrix} \mathbf{N}^+ \\ \mathbf{N}^- \end{Bmatrix}_{2(\mathrm{p}+1)} = [\mathbf{T}] \begin{Bmatrix} \mathbf{N} \\ \mathbf{NH} \end{Bmatrix}_{2(\mathrm{p}+1)}, \tag{24}$$

with a transition matrix $[\mathbf{T}]$:

$$\mathbf{T} = \frac{1}{2} \begin{bmatrix} \mathbf{I} & \mathbf{I} \\ \mathbf{I} & -\mathbf{I} \end{bmatrix}_{2(\mathrm{p}+1)\times 2(\mathrm{p}+1)}, \tag{25}$$

where $\mathbf{I}$ are identity matrices. This relation allows converting discrete quantities (elementary matrix structure) from one basis to the other, in order to take the most advantage of each basis depending on the circumstances. We will revisit this aspect in the later part. The interested reader is recommended to refer to [30, 53] for other details of equivalence and relationship between these two bases.

## 3.2. Stability analysis

In this subsection, we analyse the stability (coercivity) of the *Nitsche-type* formulation presented eq. (16) in the discrete setting $p \in \mathcal{P}_h$ (high-order X-FEM using a Heaviside enrichment) such that:

$$a_\lambda(q_h, p_h) = \ell(q_h) \quad \forall q_h \in \mathcal{P}_h, \tag{26}$$

in which a clever definition of $\lambda$ on interface integral is proposed:

$$\lambda = \left( \frac{1}{\beta_h} + \frac{\sigma d}{\mathrm{j}\omega} \right)^{-1}, \tag{27}$$

where $\beta_h$ is a discretization-dependent parameter for which both mesh configuration and approximation order have been taken into account. Unlike the expressions presented in [47, 44], the element size $h$ is already accounted implicitly here through $\beta_h$ to accommodate the high order approximation and non-matching discretization across the interface. To ensure the stability of the entire weak formulation $a_\lambda$, parameter $\beta_h$ must satisfy a specific condition that is elaborated in theorem 3.4 and proved in the following analysis.

Such a definition of $\lambda$ provides a natural transition between two extreme cases as well: When the interface parameters vanish ($\sigma d/\omega = 0$), the whole discrete formulation turns into the standard Nitsche's formulation to enforce continuity (with stability parameter as $\beta_h$). While for $\beta_h \to \infty$, the formulation tends to the *penalty-type* one.

The main ideas of the proof follow the principle described in [44], but with several differences that are originality of this paper: (i) the effect of complex-valued materials has to be considered in the proof and (ii) a high-order X-FEM approximation is used.

For the sake of analysis, the bilinear form $a_\lambda$ is rewritten in the following way:

$$\begin{aligned} a_\lambda(q_h, p_h) = a_B(q_h, p_h) &- \int_{\Gamma^*} \left(1 - \lambda \frac{\sigma d}{\mathrm{j}\omega}\right) [\![q_h]\!] \left\langle \frac{1}{\rho} \frac{\partial p_h}{\partial n} \right\rangle_\gamma \mathrm{d}S - \int_{\Gamma^*} \left(1 - \lambda \frac{\sigma d}{\mathrm{j}\omega}\right) [\![p_h]\!] \left\langle \frac{1}{\rho} \frac{\partial q_h}{\partial n} \right\rangle_\gamma \mathrm{d}S \\ &- \int_{\Gamma^*} \frac{\sigma d}{\mathrm{j}\omega} \left(1 - \lambda \frac{\sigma d}{\mathrm{j}\omega}\right) \left\langle \frac{1}{\rho} \frac{\partial q_h}{\partial n} \right\rangle_\gamma \left\langle \frac{1}{\rho} \frac{\partial p_h}{\partial n} \right\rangle_\gamma \mathrm{d}S + \int_{\Gamma^*} \lambda [\![q_h]\!] [\![p_h]\!] \mathrm{d}S. \end{aligned} \tag{28}$$

And, two discretization-dependent norms need to be defined as:

$$\|p_h\|^2 = \sum_i^2 \left( \left| \frac{\omega^2}{K_i} \right| \int_{\Omega_i} |p_h|^2 \mathrm{d}\Omega \right) \tag{29a}$$

$$|||p_h|||^2 = \sum_i^2 \left( \left| \frac{1}{\rho_i} \right| \int_{\Omega_i} |\boldsymbol{\nabla} p_h|^2 \mathrm{d}\Omega + \left| \frac{\omega^2}{K_i} \right| \int_{\Omega_i} |p_h|^2 \mathrm{d}\Omega \right) + \frac{1}{\beta_h} \int_{\Gamma^*} \left| \left\langle \frac{1}{\rho} \frac{\partial p_h}{\partial n} \right\rangle_\gamma \right|^2 \mathrm{d}S + \int_{\Gamma^*} |\lambda| \, |[\![p_h]\!].|^2 \mathrm{d}S, \tag{29b}$$

where the value of $\beta_h$, as aforementioned, depends on the mesh configuration and approximation order. The detailed proofs of the subsequent lemmas and theorems are provided in A, we state only the most influential conclusions here.

**Lemma 3.1.** *Let $\beta_h > 0$, the function $\lambda$ in definition eq. (27) satisfies:*

$$0 < |\lambda| \leq \beta_h, \tag{30a}$$

$$1 - \lambda \frac{\sigma d}{\mathrm{j}\omega} = \frac{\lambda}{\beta_h}, \tag{30b}$$

$$\left| \frac{\sigma d}{\mathrm{j}\omega} \left(1 - \frac{\sigma d}{\mathrm{j}\omega}\right) \right| \leq \frac{2}{\beta_h}, \tag{30c}$$

$$\mathrm{Re}\,(\lambda) + \mathrm{Im}\,(\lambda) - \frac{1}{2}|\lambda| \geq \frac{1}{2}|\lambda|. \tag{30d}$$

**Lemma 3.2.** *The imaginary part of the bilinear form $a_B$ in $a_\lambda$ satisfies* $\mathrm{Im}\,(a_B(\bar{p}_h, p_h)) > 0, \quad \forall p_h \in \mathcal{P}_h$

**Proof**

$$\mathrm{Im}\,(a_B(\bar{p}_h, p_h)) = \sum_i^2 \mathrm{Im}\left(\frac{1}{\rho_i}\right) \int_{\Omega_i} |\boldsymbol{\nabla} p_h|^2 \mathrm{d}\Omega - \sum_i^2 \mathrm{Im}\left(\frac{\omega^2}{K_i}\right) \int_{\Omega_i} |p_h|^2 \mathrm{d}\Omega. \tag{31}$$

It is known that for porous materials, the effective density $\rho$ has a negative imaginary part and the effective compressibility $K$ has a positive imaginary part so that damping due to thermal and viscous effects can be introduced. Therefore, we have $\mathrm{Im}\,(1/\rho_i) \geq 0$ and $\mathrm{Im}\left(\omega^2/K\right) \leq 0$, the positivity of the whole term holds. □

**Lemma 3.3.** *There exists a discretization-dependent constant $C_I$ such that (discrete inverse inequality):*

$$\int_{\Gamma^*} \left| \left\langle \frac{1}{\rho} \frac{\partial p_h}{\partial n} \right\rangle_\gamma \right|^2 \mathrm{d}S \leq C_I \sum_i^2 \int_{\Omega_i} \left| \frac{1}{\rho_i} \right| \left| \boldsymbol{\nabla} p_h \right|^2 \mathrm{d}\Omega, \tag{32}$$

*where $C_I$ depends on the polynomial approximation order and mesh regularity. This constant can be obtained by solving generalized eigenvalue problems that will be presented in the following section.*

With lemmas 3.1–3.3, the stability of the proposed formulation $a_\lambda$ in the X-FEM discrete space can be proven by the following theorem 3.4.

**Theorem 3.4.** *For any $\beta_h \geq 16\, C_I$, where $C_I$ is the constant in lemma 3.3, the bilinear form $a_\lambda$ satisfies :*

$$|a_\lambda(p_h, p_h)| + \|p_h\|^2 \geq \frac{1}{4} |||p_h|||^2, \quad \forall p_h \in \mathcal{P}_h, \tag{33}$$

which is the Gårding inequality that proves the coercivity of the variational formulation of the Helmholtz equations.

Up to here, we proved that if $\beta_h \geq 16\, C_I$ is set, the discrete *Nitsche-type* formulation is coercive. The following question is how to evaluate the constant $C_I$ in our discrete setup.

## 3.3. Estimation of the stabilization parameters: classical strategy

Parameter $\beta_h$ in the complex function $\lambda$ affects the stability of the proposed Nitsche's formulation, and has to satisfy $\beta_h \geq 16\, C_I$. Constant $C_I$ in the inverse inequality eq. (32) is associated to the eigenvalues of a generalized eigenvalue problem proposed by [41] as:

$$\mathbf{A}\mathbf{x} = \alpha \mathbf{B}\mathbf{x}, \tag{34}$$

with matrices $\mathbf{A}$ and $\mathbf{B}$ are, in the scope of our problem:

$$[\mathbf{A}]_{ij} = \int_{\Gamma_e^*} \left( \left\langle \left| \frac{1}{\rho} \right| \boldsymbol{\nabla} N_i \right\rangle_\gamma .\mathbf{n} \right) \left( \left\langle \left| \frac{1}{\rho} \right| \boldsymbol{\nabla} N_j \right\rangle_\gamma .\mathbf{n} \right) \mathrm{d}S, \tag{35a}$$

$$[\mathbf{B}]_{ij} = \int_{\Omega_e} \left| \frac{1}{\rho_i} \right| \boldsymbol{\nabla} N_i \boldsymbol{\nabla} N_j \, \mathrm{d}\Omega, \tag{35b}$$

where the weighting parameters $\gamma_i$ need to be fixed *a priori*, and are chosen as $\gamma_1 = \gamma_2 = 0.5$ for the classical Nitsche's method. Then, the eigenvalue problem can be solved globally as proposed in [18] or locally for each element as [37]. Hereinafter, the solving procedure at the element-level is presented.

In the case where a strong discontinuity is introduced into the approximation space, matrix $\mathbf{B}$ is singular with *two* zero eigenvalues (corresponding to the rigid body motions of two subdomains separated by the interface). The associated null space is also the null space of $\mathbf{A}$, which leads to indeterminate eigenvalues that cannot be used to stabilize the formulation. The deflation procedure proposed in [42] needs to be performed first. Unlike with Cut-FEM basis where $\mathbf{B}$ has two independent diagonal blocks by construction, we have a fully coupled matrix when using the X-FEM basis. The null space of $\mathbf{B}$ corresponds to rigid body modes, which can be obtained *a priori* in certain cases [1]. Herein, for a high order Heaviside-enriched X-FEM discretization, we provide the common null space basis vectors $\tilde{\mathbf{x}}$ for these two matrices for two-dimensional triangular elements with the arrangement of degree of freedom eq. (24) as [2]:

$$\tilde{\mathbf{x}} = \left[ \begin{array}{ccccc|ccccc} 1 & 1 & ... & 1 & 1 & 0 & 0 & ... & 0 & 0 \\ 0 & 0 & ... & 0 & 0 & 1 & 1 & ... & 1 & 1 \end{array} \right]_{2\times 2(3\mathrm{p}+3)}, \tag{36}$$

where p denotes the approximation order. Entries 0 and 1 correspond to the *dofs* associated to enriched and standard shape functions. With this null space, the first and last rows, columns of matrices $\mathbf{A}$ and $\mathbf{B}$ are deleted by the deflation approach proposed in [42]. Then, $C_I$ is estimated as the largest eigenvalue of the deflated eigenvalue problem. Note that the deflated matrix $\mathbf{A}$ may remain singular, but this will not prevent one from solving the determinate eigenvalue problem.

## 3.4. Evaluation of stabilization parameter: robust strategy

The choice of weighting averages and estimation strategy for the stabilization parameter presented in the former section can unfortunately yield to overestimated values for $C_I$, which may sometimes result in large condition number in the cases where large material contrasts are involved, or when elements are cut with very small volume fractions. To alleviate such numerical issues, the so-called $\gamma$-Nitsche or weighted Nitsche was proposed by Annavarapu et al. [41]. This method was shown to be a robust for linear triangular

[1] Null space of bicubic B-splines in two dimensions is given as $\tilde{\mathbf{x}} = [1, 1, 1 \ldots]_{1\times 16}$ in [42]

[2] The null space depends as well on the polynomial type. Hierarchical polynomials will lead to a different expression compared to the one presented here for the Lagrange or Bernstein polynomials.

and tetrahedral elements. Jiang et al. [42] further extended the approach to higher order elements with help of two one-sided inequalities, such that in our case:

$$\int_{\Gamma_e^*} \frac{\partial \bar{p}}{\partial n}\frac{\partial p}{\partial n}\mathrm{d}S \leq C_1 \int_{\Omega_e^-} \boldsymbol{\nabla}\bar{p}.\boldsymbol{\nabla}p\,\mathrm{d}\Omega, \tag{37a}$$

$$\int_{\Gamma_e^*} \frac{\partial \bar{p}}{\partial n}\frac{\partial p}{\partial n}\mathrm{d}S \leq C_2 \int_{\Omega_e^+} \boldsymbol{\nabla}\bar{p}.\boldsymbol{\nabla}p\,\mathrm{d}\Omega, \tag{37b}$$

in which constants $C_i$ are also obtained as the maximum eigenvalues of two generalized eigenvalue problems associated to the above inequalities (with two matrices for each side):

$$[\mathbf{A}]^- = \int_{\Gamma_e^{*-}} (\boldsymbol{\nabla}N_i.\mathbf{n})\,.\,(\boldsymbol{\nabla}N_j.\mathbf{n})\,\mathrm{d}S, \quad [\mathbf{A}]^+ = \int_{\Gamma_e^{*+}} (\boldsymbol{\nabla}N_i.\mathbf{n})\,.\,(\boldsymbol{\nabla}N_j.\mathbf{n})\,\mathrm{d}S, \tag{38a}$$

$$[\mathbf{B}]^- = \int_{\Omega_e^-} \boldsymbol{\nabla}N_i.\boldsymbol{\nabla}N_j\,\mathrm{d}\Omega, \quad [\mathbf{B}]^+ = \int_{\Omega_e^+} \boldsymbol{\nabla}N_i.\boldsymbol{\nabla}N_j\,\mathrm{d}\Omega. \tag{38b}$$

Let us stress that the procedure proposed in Jiang et al.[42] was developed using Cut-FEM basis where the matrices originating from negative/positive sides are independent. One can readily extract the non-zero terms in bases, leading to matrices $[\mathbf{A}]^{\pm}$ and $[\mathbf{B}]^{\pm}$ each composed of one non-zero sub-matrix that only has *one* a priori known zero eigenvalue. The deflation approach is then straightforward and easy to be performed.

Here, despite the use of a one-sided quadrature strategy[3], the Heaviside enrichment couples all the *dofs* on the interface (see figure fig. 3), so that the block nature of the matrices is lost. The corresponding matrices are of size of $(2 \times 3(\mathrm{p}+1)) \times (2 \times 3(\mathrm{p}+1))$ for order p triangular elements. Such matrices have a null space of dimension *three*, which leads to a worse indeterminate eigenvalue system than before. To remove this type of singularity, a direct deflation could be conducted as with the previous strategy by eliminating three columns and rows of the original matrices by finding properly the associated null eigenvectors, respectively.

In order not to search for the null space basis for each matrix and not to perform the deflation three times, we propose to decouple the matrices and reduce their dimensions first. As we know that only half of the *dofs* would be involved in the one-sided matrix if a Cut-FEM basis was considered, the decoupling procedure relies on a conversion of basis from the Heaviside X-FEM to Cut-FEM. The relationship between these two bases are revealed by eq. (24) with the transition matrix $[\mathbf{T}]$. Therefore, when matrices $\mathbf{A}$ and $\mathbf{B}$ integrated on each side are multiplied by the transition matrix $\mathbf{T}$:

$$\mathbf{A}^{*\pm} = \mathbf{T}^{\mathrm{T}}\mathbf{A}^{\pm}\mathbf{T}, \tag{39a}$$

$$\mathbf{B}^{*\pm} = \mathbf{T}^{\mathrm{T}}\mathbf{B}^{\pm}\mathbf{T}, \tag{39b}$$

[3]Matrices $[\mathbf{B}]^{\pm}$ and $[\mathbf{A}]^{\pm}$ are integrated only on one side of the element.

it yields that the decoupled matrices are in the form:

$$\mathbf{A}^{*+} = \begin{bmatrix} \mathbf{A}^{+} & \mathbf{0} \\ \mathbf{0} & \mathbf{0} \end{bmatrix}, \quad \mathbf{A}^{*-} = \begin{bmatrix} \mathbf{0} & \mathbf{0} \\ \mathbf{0} & \mathbf{A}^{-} \end{bmatrix}, \tag{40a}$$

$$\mathbf{B}^{*+} = \begin{bmatrix} \mathbf{B}^{+} & \mathbf{0} \\ \mathbf{0} & \mathbf{0} \end{bmatrix}, \quad \mathbf{B}^{*-} = \begin{bmatrix} \mathbf{0} & \mathbf{0} \\ \mathbf{0} & \mathbf{B}^{-} \end{bmatrix}. \tag{40b}$$

Now, the dimension reduced matrices are obtained only picking the non-zero block in $\mathbf{A}^{*\pm}$, $\mathbf{B}^{*\pm}$ of size $3(\mathrm{p}+1) \times 3(\mathrm{p}+1)$ denoted by $\tilde{\mathbf{A}}^{*\pm}$ and $\tilde{\mathbf{B}}^{*\pm}$. Then, the same deflation procedure as the one presented in the former section can be applied to obtain the eigenvalue constant $C_i$. Taking the effects of materials properties into account, we give the weighting parameters:

$$\gamma_i = \frac{1/(C_i|1/\rho_i|)}{(1/(C_1|1/\rho_1|) + 1/(C_2|1/\rho_2|))}, \tag{41}$$

with this weighting parameters, the lower bound of constant $C_{I_{min}}$ is derived as:

$$C_{I_{min}} = \frac{1}{1/(C_1|1/\rho_1|) + 1/(C_2|1/\rho_2|))}, \tag{42}$$

as seen that, this choice avoids a large stability parameter for the cases where $|1/\rho_1|/|1/\rho_2| \gg 1$ (large contrast) and $C_1/C_2 \gg 1$ (small volume fraction). In fact, substituting weights eq. (41) in the global system with matrices eq. (35) and applying the classical strategy, will yield an equivalent minimum of $C_I$ as eq. (42).

## 4. Numerical examples

To verify the implementation of the proposed methods and their performances in the X-FEM discretization, we conduct a series of numerical examples. The sound dissipation media used in all problems are modelled by equivalent fluid with JCA parameters [3, 4]. The resulting material properties such as density $\rho$ are complex-valued and frequency dependence calculated from the formulas in C. Pressure jump model behaves as the interface law to represent thin acoustic resistive layers with diverse resistivity $\sigma$ and thickness $d$. All the used porous materials with their properties are summed up in table C.1. In the figures legends, the *Nitsche-type* represents formulation eq. (16) and *penalty-type* is denoted for eq. (10). Without exception, the discrete systems for the following examples are solved by a direct linear solver.

When the exact solution is available, the accuracy of the methods is assessed with errors measured in $L^2$ norm, we define a global relative error for pressure solution over the entire domain:

$$\varepsilon^{g}_{L^2} = \frac{\left( \int_\Omega \left| p^{f}_{\mathrm{XFE}} - p^{f}_{\mathrm{exa}} \right|^2 \mathrm{d}\Omega \right)^{1/2}}{\left( \int_\Omega \left| p^{f}_{\mathrm{exa}} \right|^2 \mathrm{d}\Omega \right)^{1/2}} \times 100\%, \tag{43}$$

and a measurement of derivative at the interface, the flux is evaluated as well:

$$\varepsilon^f_{L^2} = \frac{\left(\int_{\Gamma^*} \left|\boldsymbol{\nabla} p^f_{\mathrm{XFE}}.\mathbf{n} - \boldsymbol{\nabla} p^f_{\mathrm{exa}}.\mathbf{n}\right|^2 \mathrm{d}S\right)^{1/2}}{\left(\int_{\Gamma^*} \left|\boldsymbol{\nabla} p^f_{\mathrm{exa}}.\mathbf{n}\right|^2 \mathrm{d}S\right)^{1/2}} \times 100\%, \tag{44}$$

where the $p^f_{\mathrm{exa}}$ represents the exact (analytical) pressure.

The mesh resolution is normally indicated by the number of *dofs* per wave-number $D_\lambda$ in the time-harmonic problems instead of mesh size $h$, such that:

$$D_\lambda = \frac{2\pi}{k^*}\sqrt{\frac{N_{\mathrm{dof}}}{\mathrm{area}(\Omega)}}, \tag{45}$$

where $k^*$ is the largest absolute value of wave numbers of two media. $N_{\mathrm{dof}}$ denotes the total number of *dofs* and area($\Omega$) is the measure of the computational domain.

## 4.1. Planar interface

### 4.1.1. Equivalent 1D problem: impedance tube

We first begin with a simple impedance tube problem, which is a common configuration to characterize porous materials. A normal unit velocity at $2,000$ Hz is prescribed on the left end of the tube and a rigid wall is set at the right end as depicted in fig. 4. The air and a plastic foam are set as the two media in the tube, between which a perfect interface or an imperfect interface modelling a resistive film are both to be simulated. As the wave propagates only in the horizontal direction, the waveform depends only on $x$, so that a one-dimensional mesh $\Omega = [-1, 1]$ is sufficient to obtain the solution. The interface is located at $x = 0$ and only cuts the central element of the mesh.

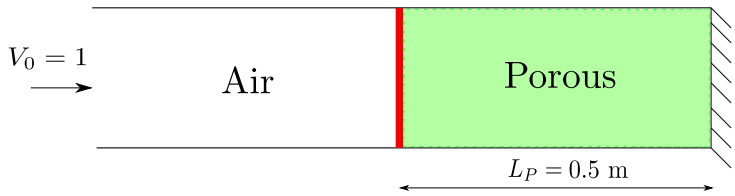


Figure 4: Illustration of the impedance tube problem

Note that only the *Nitsche-type* formulation is able to handle the perfect interface condition case. When a thin woven film with flow resistivity $\sigma = 775.10^3$ N s m$^{-4}$ and thickness $d = 1$ mm is inserted at the interface, both *Nitsche* and *penalty-type* formulations can account for the pressure drop caused by the film. Fig. 5 shows the real part solution for two types of interfaces, numerical solutions are obtained with $D_\lambda = 60$. An obvious and progressive attenuation of the pressure is observed for both solutions for

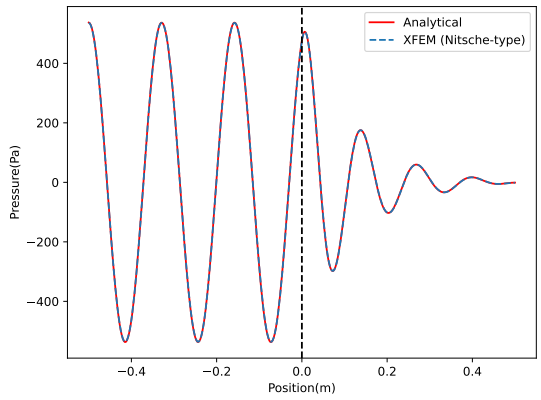


(a)

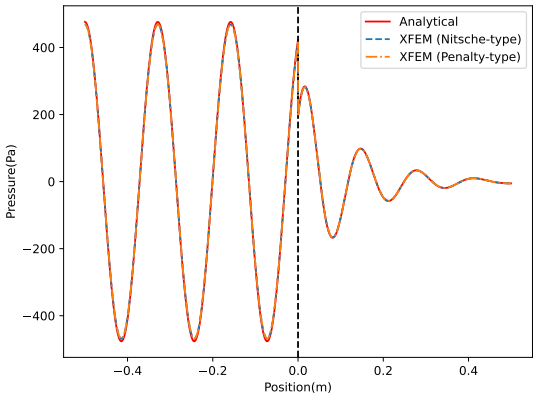


(b)

Figure 5: Real part of pressure solution (in Pa) for (a) perfect interface problem ($\sigma d = 0$) and (b) imperfect interface $\sigma d = 775$ N s m$^{-3}$ at 2,000 Hz.

$x > 0$ because of the plastic foam. All the numerical solutions are in great qualitative agreement with the analytical ones.

In order to further quantify the numerical properties of the proposed method, the convergence is to be examined. Before that, the sensitivity of the accuracy to variations in the stability parameter $\beta_h$ needs to be identified for *Nitsche-type* formulation. This allows us to corroborate the stability criterion that was derived from the coercivity proof. We solve the same problems, conducting a set of numerical experiments through sweeping the value of $\beta_h$ using the same discretization $D_\lambda$. Global errors are evaluated in fig. 6 for perfect and imperfect interface. For both types of interface, a 'spike' in the error is observed, for values of $\beta_h$ very close to the constant $C_I$ (calculated from the problem-independent generalized eigenvalue problem eq. (34)).The region around this spike is deemed 'unstable', as the solution error varies significantly. Then, there exists a quite large range of $\beta_h$ where the error remains 'optimal', which implies that the choice of

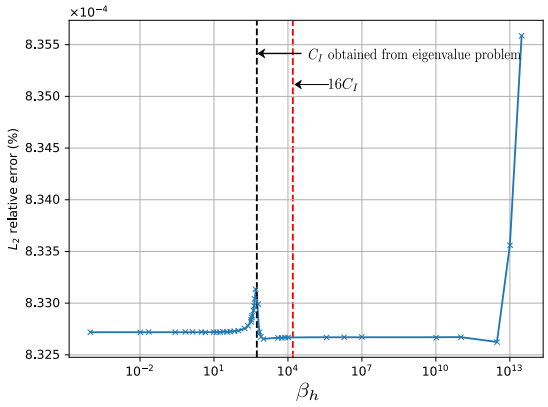


(a)

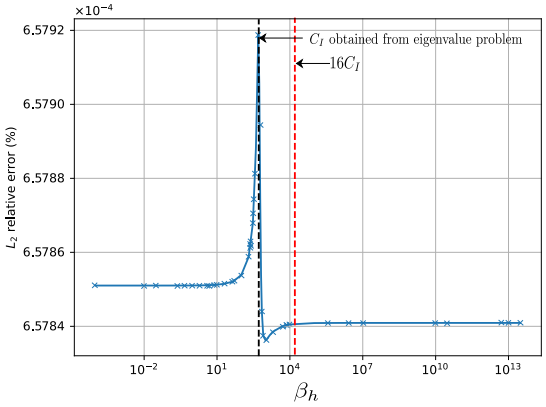


(b)

Figure 6: Sensitivity of the relative error to the stability parameter $\beta_h$ in function $\lambda$ for (a) perfect interface and (b) imperfect interface ($\sigma d = 775$ N s m$^{-3}$).

the stability parameter is not very restrictive in regard to obtaining an accurate solution. It is seen that $16C_I$, which is the lower bound of our stability condition obtained from previous theoretical analysis, is slightly greater than $\beta_h$ at the 'spike' and located within the stable region. This result verifies our proof of stability, which requires $\beta_h \geq 16C_I$. It is noted that similar curves have also been reported in [54].

We notice that for perfect interface fig. 6(a), the error starts to increase beyond $\beta_h \simeq 10^{13}$, which is because the large stability parameter begins to violate the whole formulation. On the contrary, for the imperfect case fig. 6(b), a 'constant' error is observed over the entire range of tested $\beta_h$. This is due to the definition of $\lambda$ eq. (27) which includes $\mathrm{j}\omega/\sigma d$ that bounds the formulation when $\beta_h$ keeps increasing.

Now, we monitor the convergence of the proposed method for the perfect and imperfect interface cases with prescribed physical parameters. $h$-refinement is conducted

with a base discretization where $D_\lambda = 1$ and split the mesh sequentially six times under linear, quadratic, cubic and quartic approximations respectively. p-refinement is also performed by increasing interpolation order until $\mathrm{p} = 10$ with the base mesh. The stabilization parameter is chosen as $\beta_h = 16C_I$, with $C_I$ calculated by the robust strategy described in section 3.4. Fig. 7 shows convergence curves of the relative global error for the two interface types. Optimal rates of convergence $\mathcal{O}(h^{-(\mathrm{p}+1)})$ are reached for every polynomial degree after a pre-asymptotic stage where the known *rule of thumb* ($8-10$ *dofs* per wavelength for a linear element to obtain a reliable result) is also verified. Moreover, p-refinement, as expected, exhibits an exponential rate of convergence compared to $h$-refined, as reported in [11] for the Helmholtz equation.

The conditioning of the general global stiffness matrix is also worth being assessed, as it is associated with the stability and efficiency of the resolution procedure. The variation of the condition number of the global matrix with respect to $\beta_h$ for different $\sigma d$ is plotted in fig. 8. First, small 'spikes' on the conditioning close to the constant $C_I$ are observed, as well as in the global error for all $\sigma d$. Second, all the condition numbers tend to an asymptotic value when $\beta_h$ is large enough. In fact, these asymptotic condition numbers correspond exactly to those of the *penalty-type* formulation, implying that the conditioning of the proposed *Nitsche-type* is also bounded for imperfect interfaces.

In contrary to the global error shown previously, the condition number is more sensitive to $\beta_h$ when $\sigma d$ is smaller. The stability parameter $\beta_h$ may not be chosen too large in order to avoid ill-conditioned linear systems. We observe that the *Nitsche-type* formulation offers a stable conditioning when the stability parameter is chosen near $\beta_h = 16C_I$. In addition to the global error plot fig. 6, the lower bound of $\beta_h$ seems to be the best choice for the stability parameter in order to obtain an 'optimal' solution in terms of accuracy and conditioning.

Finally, it is known that penalty methods may suffer from ill-conditioning and cannot offer a converged solution when the penalization parameter becomes very large. This issue drives us to investigate the behaviour of the proposed *Nitsche-type* formulation with the optimal stability parameter for near-perfect interface cases. The convergence and conditioning of the formulation under a $h$-refinement are examined for three gradually decreasing $\sigma d$ in fig. 9. The curves for the *penalty-type* formulation are also depicted for comparison.

The curves corresponding to the *Nitsche-type* formulations are all superimposed for both convergence and condition number. Furthermore, optimal convergence rates are preserved. Regarding the *penalty-type* results, optimal convergence is only maintained for $\sigma d = 1.10^{-5}\ \mathrm{N\,s\,m^{-3}}$, and is completely degraded for $\sigma d = 1.10^{-15}\ \mathrm{N\,s\,m^{-3}}$ beyond certain $D_\lambda$. In addition, the *penalty-type* condition numbers are all larger than the corresponding ones using the *Nitsche-type* formulation. In the literature, these poor convergences are usually attributed to the ill-conditioning of the system [28]. We emphasize that the condition numbers does not increase significantly here (and even decrease) during the $h$-refinement (see fig. 9(b)). In addition, although these conditioning is much higher, converged solutions should still be obtained when a direct solver is used. Hence, the conditioning should not be the main reason leading for such a poor convergence of the solution. It is more probably because under these pressure jump parameters, inter-

face conditions are enforced too strictly to be able to cope with the other bulk terms in the formulation when a very large penalization parameter is selected. We will revisit this aspect in two-dimension meshed problems to verify this conclusion. Nevertheless, the proposed *Nitsche-type* formulation shows excellent performances for any pressure jump parameters.

#### 4.1.2. Oblique incident wave problem

To validate the conclusions from the uni-dimensional problem presented in the previous section and to account for the effects of mesh configuration, we consider herein a classical two-dimensional benchmark as used in [55]. An oblique incident plane wave of unit amplitude propagates in an infinite plane from air to a foam coated with a thin acoustic layer at $x = 0$. The foam medium is modelled by JCA equivalent fluid once more, and the pressure jump condition is prescribed at the interface to represent the thin layer. The analytical solution for such a problem is obtained by solving reflection $R$ and transmission $T$ with the interface condition in eq. (4), which is provided in D.

The computational domain $\Omega$ is a square of $[-0.25, 0.25] \times [0, 0.5]$ m$^2$ discretized by means of an unstructured triangular mesh, as illustrated in fig. 10(a). It is clear that in such mesh, the interface intersects with elements arbitrarily, which allows us to test the robustness of methods with respect to cut elements. Concerning the boundary conditions, the exact velocity (Neumann) is prescribed on the four external boundaries. Fig. 10(b) depicts the real part of the pressure field using such mesh, and solved by the *Nitsche-type* X-FEM. An incident plane wave tilted by $\pi/4$ rads at $2,000$ Hz is modelled, and an imperfect interface with $\sigma d = 775.10^3 \times 1.10^{-3}$ N s m$^{-3}$ is considered. Aside from the attenuation and drop of the pressure observed in 1D configuration, a change of propagation direction is also observed at the interface due to the material heterogeneity.

For the proposed *Nitsche-type* formulation, the stability parameter has first to be computed. To highlight the difference between the classical and robust strategies proposed in section 3 when material heterogeneity [4] and small cuts are involved, we illustrate in fig. 11 the element-wise stabilization parameter ($\beta_h = 16C_I$) along the interface, estimated by the two strategies and considering a cubic polynomial approximation. In general, the classical strategy provides larger $\beta_h$ than the robust one. The element with the smallest cut portion leads to the largest stability parameters (deep red in fig. 11(a)), which is consistent with what was observed using the classical Nitsche method. By contrast, the robust strategy averages the two constants $C_i$ on each side with appropriate weightings, yielding a much smaller stability parameter (deep blue in fig. 11(b)) for the same element. In fact, the stability parameter can be controlled in a reasonable range even when the interface is extremely close to the element boundary, while the one evaluated by the classical strategy will explode, resulting in conditioning issue [5]. It is worth reminding that for Nitsche's method, increasing the stability parameter by one or two orders of magnitude (as observed here) does not lead to any incorrect or

[4] The density of air and considered foam are respectively $|\rho_a| = 1.213$ kg m$^3$, $|\rho_f| = 29.4$ kg m$^3$

[5] The evolution of constant $C_I$ against the relative position of the interface inside 1D elements is provided in B for completeness

non-converged solution, as discussed previously. However, for problems involving a large contrast in the material properties (for instance a $10^{10}$ ratio as investigated in [42]), classical Nitsche's method will lead to deteriorated results. Although we are not in the case of such large materials contrast, the robust strategy for computing the stability parameter $\beta_h$ is employed, without exception, for all the following calculations to obtain the 'optimal' performance of the *Nitsche-type* formulation. We refer the interested reader to [42] and [41] for in-depth studies on the influence of the interface location and material contrast within Nitsche's method.

The convergence is now analyzed: in addition to the global error over the domain, the average flux across the two sides of the interface is also evaluated to assess the local accuracy of the dual variable. For the sake of brevity, only the results for $\mathrm{p} = 3$ are presented. Figs. 12(a) and 12(b) present the convergence curves for perfect and imperfect interfaces with realistic film parameters ($\sigma d = 775\ \mathrm{N\,s\,m^{-3}}$). The *Nitsche-type* formulation achieves an optimal rate regarding both global solution $\mathcal{O}(h^{-(\mathrm{p}+1)})$ and average interfacial flux $\mathcal{O}(h^{-\mathrm{p}})$ for the two types of interface conditions. The *penalty-type* formulation is not able to enforce the perfect interface condition, but exhibits a similar convergence behaviour as the *Nitsche-type* for imperfect interface. As for the previous numerical example, we compare the convergence behaviour of the two formulations for near-perfect interfaces such when $\sigma d = 1.10^{-15}\ \mathrm{N\,s\,m^{-3}}$, shown in fig. 12(c). The *Nitsche-type* formulation can still give an optimal convergence with an error level similar to the two previous interface conditions. However, both global solution and interfacial flux fail to converge when the *penalty-type* approach is used. These curves confirm the conclusions drawn from the 1D configuration.

We now try to identify how does the *Nitsche-type* formulation behave with respect to the interface parameters $\sigma d$, and also explain the divergence of the solution with the *penalty-type* formulation for small $\sigma d$. The variation of solution accuracy and conditioning of the discrete system are thus evaluated with decreasing $\sigma d$.

In order to focus on the solution at the interface, we define two additional error indicators at the interface that are the local pressure error along the interface:

$$\varepsilon^l_{L^2} = \frac{\left(\int_{\Gamma^*} \left|p_{\mathrm{XFE}} - p_{\mathrm{ref}}\right|^2 \mathrm{d}S\right)^{1/2}}{\left(\int_{\Gamma^*} \left|p_{\mathrm{ref}}\right|^2 \mathrm{d}S\right)^{1/2}} \times 100\%, \tag{46}$$

and the local pressure jump error $[\![p]\!]$:

$$\varepsilon^j_{L^2} = \left(\int_{\Gamma^*} \left|[\![p]\!]_{\mathrm{XFE}} - [\![p]\!]_{\mathrm{ref}}\right|^2 dS\right)^{1/2}. \tag{47}$$

Note that the value of $[\![p]\!]_{\mathrm{ref}}$ varies (decreases) with respect to $\sigma d$. Therefore, in order to avoid a large error indicator, the absolute error rather than relative error is calculated for the pressure jump.

Fig. 13 plots the relative average pressure error, average interfacial flux error, absolute pressure jump error and condition number computed in the asymptotic stage (fourth

point in fig. 12) as a function of $(\sigma d)^{-1}$. The effects of the frequency are considered as well in this study by taking a low 10 Hz and a medium $1,000$ Hz frequency excitation. We recall that the frequency has an influence on the whole solution, as the properties of the JCA model and the interface jump behaviour are frequency-dependent.

It can be observed that for all metrics the *Nitsche-type* formulation with the 'optimal' stability parameter delivers, as expected, a stable trend over the entire range of interface parameters. Moreover, it exhibits a marginally lower error level in a large range of interface parameter compared to the *penalty-type* formulation for local pressure value fig. 13(a) and the interfacial flux fig. 13(b), especially under the low frequency excitation.

Interestingly, the curves corresponding to the *penalty* case exhibit two distinct regimes for these metrics. Regarding the local pressure and interfacial flux, it gives an accuracy which is similar to the *Nitsche-type* formulation at the beginning until about $(\sigma d)^{-1} = 10^{10}$, where the condition numbers are slightly larger. Then, from $(\sigma d)^{-1} = 10^{10}$ to $10^{14}$, the error increases brutally, while its conditioning is still in a reasonable range for which the direct linear solver should be able to give an accurate solution. After $(\sigma d)^{-1} = 10^{14}$, even if the conditioning keeps increasing with a linear rate, the error remains almost constant. It is seen that there is no strong correlation between convergence loss and conditioning for the *penalty-type* formulation.

When it comes to the error in the pressure jump condition, errors for the *penalty-type* case continue to decrease with a linear rate after a short range of superimposition with *Nitsche-type* until around $(\sigma d)^{-1} = 10^{6} - 10^{10}$, and after that the error stays constant. This phenomenon indicates that the physical parameters in the interface term of the *penalty-type* formulation not only determine the value of pressure jump, but also work as a penalization to enforce the interface condition. The larger the penalty parameter is, the better the interface condition is enforced. However, this 'better' imposition only seek to enforce the pressure jump $[\![p]\!]$ at the interface, at the expense of the rest of the physics. When $\sigma d$ is beyond a specific value ($10^{10}$ here), the limit of accuracy for the pressure jump is reached, and larger $\sigma d$ solely makes the elementary matrices along the interface too stiff to represent the whole solution properly. Then, when $(\sigma d)^{-1}$ becomes sufficiently large, the interface integral takes control of the behaviour of the whole formulation. This also explains the linear increase of the condition number in the range of constant error in the pressure jump.

In summary, the proposed *Nitsche-type* formulation within X-FEM presents stability in terms of accuracy and conditioning with respect to the interface parameters. In addition, the prediction of the interfacial flux is more accurate than with the *penalty-type* formulation. Although there exists a wide range of $\sigma d$ (under a fixed frequency), where the *penalty-type* formulation shows a similar accuracy as the Nitsche's one, it should be noticed that this range might change with regard to frequency and material properties. Therefore, in order to avoid unexpected results for some specific problem setups, the *Nitsche-type* formulation is recommended.

## 4.2. Curved interface: cylinder scattering problem

We now consider a two-dimensional cylinder scattering problem where a cylindrical porous material made of a classical foam is surrounded by an infinite air media. At the interface, a null-thickness thin layer is considered as well. This example provides a more complicated scenario to assess the performance of the proposed methods. The presence of curved interfaces requires more effort to represent the geometry, reducing the influence of the geometrical error in the finite element approximation. The analytical solution of such sound radiation in the free field involves complex-valued Hankel and Bessel functions and is provided in D.

The computational domain is defined as $\Omega = [-0.25, 0.25] \times [-0.25, 0.25]$ m$^2$ meshed with triangular elements. Exact velocities are prescribed as Neumann boundary condition on the outer boundaries. The scatterer profile (circle of radius 0.12 m at $x = 0$) is described by a piece-wise linear level-set function. In order to recover the optimal rate of convergence with the high-order approximation, such level-set is defined on a refined geometrical mesh. Fig. 14(a) illustrates the problem set-up and the three times locally refined mesh for the geometry of the circle. We recall that although the level-set is defined on the refined mesh, the approximation of the solution is still performed on the uniform coarse mesh. The detailed relationship between approximation and geometric mesh size can be found in [50, 42]. Fig. 14(b) illustrates the solution using the *Nitsche-type* X-FEM and the corresponding mesh. It corresponds to the propagation of a plane wave in an infinite domain at $2,000$ Hz which interacts with the porous scatterer on which a woven film ($\sigma d = 775$ N s m$^{-3}$) is attached. Both dissipation and discontinuity of the pressure at the interface are successfully captured on this relatively coarse mesh thanks to quartic elements.

Again, the convergence analysis is carried out within the proposed framework, and compared to the results obtained by the *penalty-type* formulation. Fig. 15 plots the convergence of the $L^2$ norm of the relative global error and average interfacial error for p = 3. For the parameters corresponding to a woven film at the interface in fig. 15(a), the two formulations lead to identically optimal convergence rates for the two accuracy indicators. These results also demonstrate that optimal convergence rates can be obtained when the geometric error is mastered. As in the previous examples, near-perfect interface conditions are also tested, as shown in fig. 15(b). Optimal convergences are still obtained using the *Nitsche-type* formulation and maintain an error level which is similar to the imperfect interface. Like for the planar interface, the *penalty-type* formulation is not able to converge with these near-perfect interface parameters.

## 4.3. Application to car cavity problem

In this final example, we test the proposed method to predict a more realistic acoustic field in a relatively larger domain $\Omega \in \mathbb{R}^2$. The problem consists of a car cavity full of air with a dimension of 2.67 m $\times$ 1.1 m and a driver seat made of porous XFM material (eXtra Firm Mattress). The sound field is generated through imposing an arbitrary normal velocity ($\partial p/\partial n = 1$) on the front windscreen. As the analytical solution does

not exist for this problem, the problem is solved using an interface-fitted mesh that serves as a reference. The geometry of the model and used meshes are depicted in fig. 16. Fig. 16(a) displays that within interface-fitted FEM, a sufficient amount of elements is necessary to conform to the boundary of the interface and describe the small geometrical features (top of the seat). This is in stark contrast with the X-FEM where the geometry of the seat is independent of the elements. The geometry is then defined implicitly by a set of linear level-set functions (see fig. 16(b)). The mesh used for the X-FEM has a comparable element size with respect to its conventional interface-fitted counterpart. In order to avoid changing the mesh to obtain a converged solution, we increase the polynomial degree p (p-refinement) for both methods.

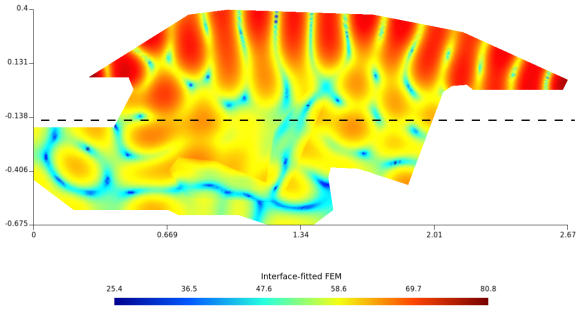


(a)

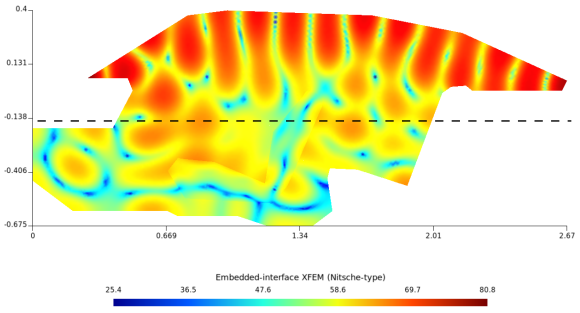


(b)

Figure 17: Snapshots of the numerical solution (pressure in dB) for (a) interface-fitted FEM with *penalty-type* formulation and (b) embedded interface X-FEM with *Nitsche-type* formulation.

The effect of the thin porous layers under an excitation frequency of $1,000$ Hz is first assessed. A high resistive foam ($\sigma = 57.10^3$ N s m$^{-4}$) of thickness $d = 3$ mm is attached on the driver seat, which is accounted by the pressure jump model as an interface condition. The solutions for a perfect interface ($\sigma d = 0$) are also calculated for the purpose of comparison. For the interface-fitted FEM, double nodes are created at the interface to represent the discontinuity, and a *penalty-type* formulation is employed

to impose the interface conditions weakly. For the interface-embedded X-FEM, both *penalty-type* and *Nitsche-type* formulations proposed previously are used to enforce the interface conditions. It is worth noticing that the *penalty-type* formulation cannot handle the perfect interface exactly: the solution has to be approximated by near-perfect parameters. Considering the magnitude of the matrix terms, which are almost around 0.1 to 1, $\sigma d = 1.10^{-15}\,\mathrm{N\,s\,m^{-3}}$ is chosen to represent a value close to zero. This value of $\sigma d$ is used for *penalty-type* in both interface-fitted FEM and interface embedded X-FEM model to verify mutually if it is able to represent the perfect interface appropriately and to give a converged solution.

Fig. 17 shows the sound pressure level (SPL) for the considered problem where the thin porous layer attached on the seat. The sound absorption in the region of the seat and distinct discontinuities at its contour are observed in the two figures. The two different discretization methods are in a very good accordance. For completeness, we provide in fig. 18 the evolution of the solution along a line in the middle of the cavity (see the black dashed line in fig. 17). The three curves (reference solution, *penalty-type* and *Nitsche-type* formulations) are superimposed in fig. 18(a). By comparing with the solutions for a perfect interface (fig. 18(b)), the pressure drop at the interface is clearer and a lower level of pressure in the seat is observed because of the coated thin layer. On the other hand, interface-fitted FEM *penalty-type* formulation using the near-perfect interface value of $\sigma d$ are in great agreement with X-FEM *Nitsche-type* formulation with $\sigma d = 0$, which validates the rationality of choosing such $\sigma d$ to represent perfect interfaces. However, for the same value of $\sigma d$, the *penalty-type* formulation within X-FEM differs with the two other solutions, particularly in the vicinity of the porous seat. As discussed previously, these gaps result from the degradation of the solution on the cut elements at the interface when the *penalty-type* formulation applied for nearly perfect interfaces.

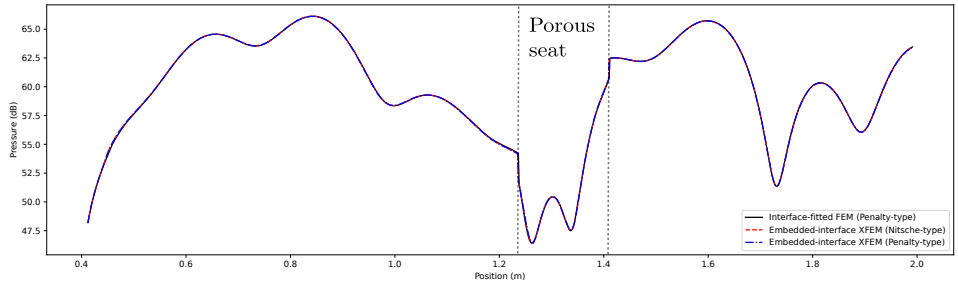


(a)

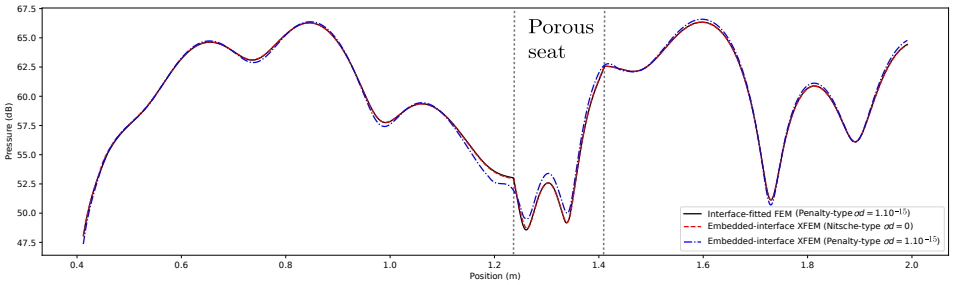


(b)

Figure 18: Comparison of the solutions on the dashed line depicted in fig. 17. (a) interface coated with a thin resistive foam ($\sigma d = 57.10^3 \times 1.10^{-3}$) (b) Perfect interface.

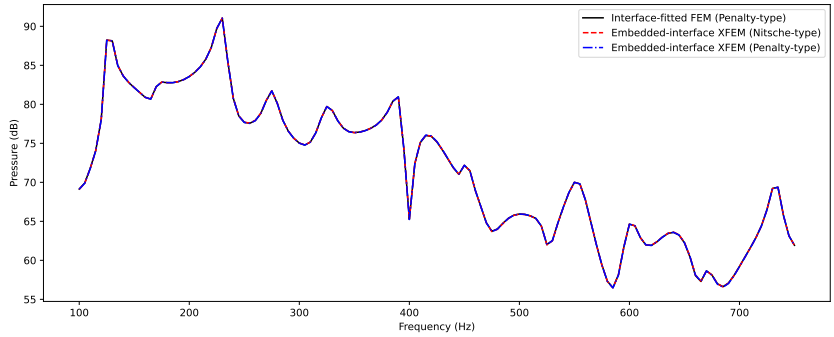


(a)

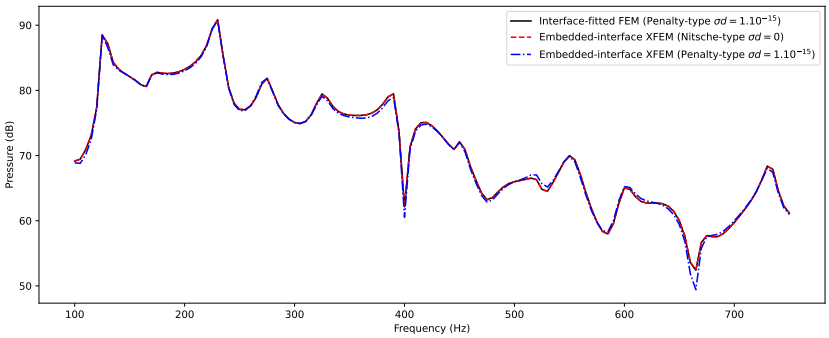


(b)

Figure 19: Frequency Response Function (a) interface coated with a thin resistive foam ($\sigma d = 57.10^3 \times 1.10^{-3}$) (b) Perfect interface.

In many situations, the frequency response is of primary importance to examine acoustic systems. It is known that the material properties of porous materials (effective density $\rho$ and bulk compressibility $K$), the interface law ($\sigma d/\omega$) and the global solution are all modified as variation of frequency in our case. Therefore, studying the solution against the frequency allows us to evaluate the robustness of the proposed method with respect to all these effects. The pressure level at the head position of the conductor (marked by a red point at $(1.17, 0.0045)$ in fig. 16) are assessed in the frequency range $f \in [100, 750]$ Hz. Again, the Frequency Response Function (FRF) is evaluated for both the coated thin layer interface and the perfect interface (see Fig. 19).

Similar with the former case, the three approaches lead to the same behaviour for a coated thin layer interface, while an obvious difference is observed for the perfect interface case. The *Nitsche-type* formulation agrees almost perfectly with the reference solution (interface-fitted FEM *penalty*) over the whole frequency range. On the contrary, the *penalty-type* within X-FEM displays a non-negligible discrepancy, bigger than 3 dB around 660 Hz especially.

## 5. Conclusions and perspectives

In this work, we explored the weak enforcement of interface laws in in-homogeneous dissipative acoustic problems, with particular emphasis on the framework of Heaviside enriched eXtended Finite Element Method (X-FEM). A general pressure jump robin-type interface condition is considered as an interface law so that it can cover the imperfect and perfect interface cases. Porous materials with complex-valued properties are the main dissipative media considered in this work.

We start by deriving a weak form of the Helmholtz equation that accounts for the pressure jump condition directly, highlighting a structure similar to the penalty method. Then, in order to handle prefect interface conditions in a common framework and to avoid the potential numerical issues, a *Nitsche-type* weak formulation is established. The relationship and conversion between these two formulations are also revealed through choosing particular values for the stability parameter. Then, we propose a discrete *Nitsche-type* formulation with a clever definition of parameter $\lambda$ on stability term, which extends the ideas already presented in [47] and [44] to dissipative in-homogeneous Helmholtz problems and relaxes meshing requirements by means of a high-order X-FEM approximation. The proof of stability for this formulation and its corresponding conditions are provided. Two strategies to determine the stability parameter in the proposed computational framework are proposed, with a highlight of the differences compared to the Cut-FEM method.

We present a set of numerical tests from 1D, 2D planar and curved interface problems to a relatively larger scale realistic application. For the *Nitsche-type* formulation, the results demonstrate that the choice of the stability parameters given from the theoretical analysis is 'optimal' in terms of accuracy and conditioning of the discrete system. Compared to the *penalty-type* formulation, the *Nitsche-type* approach with the proposed stability parameter is able to provide an equivalent or lower conditioning while maintaining the same level of accuracy. The convergence tests illustrate that the *Nitsche-type* formulation manages to achieve the 'optimal' rates for both pressure error over the domain ($\mathcal{O}(h^{-(\mathrm{p}+1)})$) and flux at the interface ($\mathcal{O}(h^{-\mathrm{p}})$) in $L^2$ norm for perfect, imperfect and nearly-imperfect interfaces ($\sigma d \to 0$). In contrast, we find that the *penalty-type* formulation is unable to converge for the cases where $\sigma d \to 0$, and that it is not related to the condition number of the discrete system.

In summary, the proposed discrete *Nitsche-type* formulation within the X-FEM is a reliable method in the sense that it is always able to provide a stable and solvable result regardless of discretization, geometry, frequency and interface parameters. Such robustness is a great advantage for parametric or optimization studies. In this paper, dissipative media were considered as equivalent fluids governed by the Helmholtz equation. Future work is expected to extend these results to the two-phase Biot's coupling governing equations [1, 2] for dissipative vibro-acoustic problems, which will leads to a fluid-solid interface. That would bring supplement challenge to prove the coercivity of the formulation and to estimate the weighting and stability parameters.

## Acknowledgement

Authors gratefully acknowledge to Prof. Anthony Nouy for the discussion on the mathematical aspects in this paper, especially the stability proof of the proposed formulation.

## A. Stability proofs for the discrete Nitsche-type formulation

**Proof**[3.1] with the definition eq. (27), right inequality in eq. (30a) follows from:

$$|\lambda^{-1}|^2 = \left|\frac{1}{\beta_h} + \frac{\sigma d}{\mathrm{j}\omega}\right|^2 = \left(\frac{\sigma d}{\omega}\right)^2 + \left(\frac{1}{\beta_h}\right)^2 \geq \frac{1}{\beta_h^2}, \tag{A.1}$$

then, and left inequality in eq. (30a) is bounded as:

$$|\lambda|^{-1} = \left|\frac{1}{\beta_h} + \frac{\sigma d}{\mathrm{j}\omega}\right| \leq \frac{1}{\beta_h} + \frac{\sigma d}{\omega}. \tag{A.2}$$

Identity eq. (30b) is obtained directly from the definition of $\lambda$. Then, the left-hand side in eq. (30c) is expressed as:

$$\frac{\sigma d}{\mathrm{j}\omega}\left(1 - \lambda\frac{\sigma d}{\mathrm{j}\omega}\right) = \frac{\sigma d}{\mathrm{j}\omega}\frac{1}{\beta_h}\lambda = \frac{1}{\beta}_h\left(\frac{1}{\beta_h} + \frac{\sigma d}{\mathrm{j}\omega} - \frac{1}{\beta_h}\right)\lambda = \frac{1}{\beta_h}\left(\lambda^{-1} - \frac{1}{\beta_h}\right)\lambda = \frac{1}{\beta_h} - \left(\frac{1}{\beta_h}\right)^2\lambda, \tag{A.3}$$

and by the triangle inequality and proved inequality eq. (30a), leads to the bound eq. (30c), that:

$$\left|\frac{\sigma d}{\mathrm{j}\omega}\left(1 - \lambda\frac{\sigma d}{\mathrm{j}\omega}\right)\right| \leq \frac{1}{\beta_h} + \left(\frac{1}{\beta_h}\right)^2|\lambda| \leq \frac{2}{\beta_h}. \tag{A.4}$$

The last inequality is given by the fact that $\sigma d$ is a real number ($\mathrm{Re}\,(\lambda) > 0, \mathrm{Im}\,(\lambda) > 0$) and $|\mathrm{Re}\,(z)| + |\mathrm{Im}\,(z)| \geq |z|$,

$$\mathrm{Re}\,(\lambda) + \mathrm{Im}\,(\lambda) - \frac{1}{2}|\lambda| = |\mathrm{Re}\,(\lambda)| + |\mathrm{Im}\,(\lambda)| - \frac{1}{2}|\lambda| \geq \frac{1}{2}|\lambda|. \tag{A.5}$$

□

**Proof**[3.4] choosing $q_h = \bar{p}_h$ as the conjugation in formulation eq. (28) yields:

$$\begin{aligned} a_\lambda(\bar{p}_h, p_h) = a_B(\bar{p}_h, p_h) &- \int_{\Gamma^*}\left(1 - \lambda\frac{\sigma d}{\mathrm{j}\omega}\right)[\![\bar{p}_h]\!]\left\langle\frac{1}{\rho}\frac{\partial p_h}{\partial n}\right\rangle_\gamma \mathrm{d}S - \int_{\Gamma^*}\left(1 - \lambda\frac{\sigma d}{\mathrm{j}\omega}\right)[\![p_h]\!]\left\langle\frac{1}{\rho}\frac{\partial \bar{p}_h}{\partial n}\right\rangle_\gamma \mathrm{d}S \\ &- \int_{\Gamma^*}\frac{\sigma d}{\mathrm{j}\omega}\left(1 - \lambda\frac{\sigma d}{\mathrm{j}\omega}\right)\left\langle\frac{1}{\rho}\frac{\partial \bar{p}_h}{\partial n}\right\rangle_\gamma\left\langle\frac{1}{\rho}\frac{\partial p_h}{\partial n}\right\rangle_\gamma \mathrm{d}S + \int_{\Gamma^*}\lambda|[\![p_h]\!]|^2\mathrm{d}S. \end{aligned} \tag{A.6}$$

Let us combine real and imaginary part of all the expression. And applying inequality $\mathrm{Re}\,(z) + \mathrm{Im}\,(z) \leq \sqrt{2}|z|$ to the second, third and fourth terms in the above equations,

we get an inequality as :

$$\begin{aligned}
&\mathrm{Re}\left(a_\lambda(\bar{p}_h,p_h)\right)+\mathrm{Im}\left(a_\lambda(\bar{p}_h,p_h)\right)\geq \mathrm{Re}\left(a_B(\bar{p}_h,p_h)\right)+\mathrm{Im}\left(a_B(\bar{p}_h,p_h)\right)\\
&-\sqrt{2}\int_{\Gamma^*}\left|\left(1-\lambda\frac{\sigma d}{\mathrm{j}\omega}\right)\right|\left|[\![\bar{p}_h]\!]\left\langle\frac{1}{\rho}\frac{\partial p_h}{\partial n}\right\rangle_\gamma\right|\mathrm{d}S-\sqrt{2}\int_{\Gamma^*}\left|\left(1-\lambda\frac{\sigma d}{\mathrm{j}\omega}\right)\right|\left|[\![p_h]\!]\left\langle\frac{1}{\rho}\frac{\partial \bar{p}_h}{\partial n}\right\rangle_\gamma\right|\mathrm{d}S\\
&-\sqrt{2}\int_{\Gamma^*}\left|\frac{\sigma d}{\mathrm{j}\omega}\left(1-\lambda\frac{\sigma d}{\mathrm{j}\omega}\right)\right|\left|\left\langle\frac{1}{\rho}\frac{\partial \bar{p}_h}{\partial n}\right\rangle_\gamma\left\langle\frac{1}{\rho}\frac{\partial p_h}{\partial n}\right\rangle_\gamma\right|\mathrm{d}S+\int_{\Gamma^*}\left(\mathrm{Re}\left(\lambda\right)+\mathrm{Im}\left(\lambda\right)\right)|[\![p_h]\!]|^2\mathrm{d}S\\
&=\mathrm{Re}\left(a_B(\bar{p}_h,p_h)\right)+\mathrm{Im}\left(a_B(\bar{p}_h,p_h)\right)-2\sqrt{2}\int_{\Gamma^*}\left|\left(1-\lambda\frac{\sigma d}{\mathrm{j}\omega}\right)\right|\left|[\![p]\!]\left\langle\frac{1}{\rho}\frac{\partial p_h}{\partial n}\right\rangle_\gamma\right|\mathrm{d}S\\
&-\sqrt{2}\int_{\Gamma^*}\left|\frac{\sigma d}{\mathrm{j}\omega}\left(1-\lambda\frac{\sigma d}{\mathrm{j}\omega}\right)\right|\left|\left\langle\frac{1}{\rho}\frac{\partial p_h}{\partial n}\right\rangle_\gamma\right|^2\mathrm{d}S+\int_{\Gamma^*}\left(\mathrm{Re}\left(\lambda\right)+\mathrm{Im}\left(\lambda\right)\right)|[\![p_h]\!]|^2\mathrm{d}S,
\end{aligned}\tag{A.7}$$

and also with the lemma 3.2, we have

$$\mathrm{Re}\left(a_B\right)+\mathrm{Im}\left(a_B\right)\geq|a_B|,\tag{A.8}$$

which leads to the following inequality:

$$\begin{aligned}
\mathrm{Re}\left(a_\lambda(\bar{p}_h,p_h)\right)+\mathrm{Im}\left(a_\lambda(\bar{p}_h,p_h)\right)&\geq|a_B(\bar{p}_h,p_h)|-2\sqrt{2}\int_{\Gamma^*}\left|\left(1-\lambda\frac{\sigma d}{\mathrm{j}\omega}\right)\right|\left|[\![p_h]\!]\left\langle\frac{1}{\rho}\frac{\partial p_h}{\partial n}\right\rangle_\gamma\right|\mathrm{d}S\\
&-\sqrt{2}\int_{\Gamma^*}\left|\frac{\sigma d}{\mathrm{j}\omega}\left(1-\lambda\frac{\sigma d}{\mathrm{j}\omega}\right)\right|\left|\left\langle\frac{1}{\rho}\frac{\partial p_h}{\partial n}\right\rangle_\gamma\right|^2\mathrm{d}S+\int_{\Gamma^*}\left(\mathrm{Re}\left(\lambda\right)+\mathrm{Im}\left(\lambda\right)\right)|[\![p_h]\!]|^2\mathrm{d}S.
\end{aligned}\tag{A.9}$$

For the second term in the above equation with identity in eq. (30b), we get:

$$2\sqrt{2}\int_{\Gamma^*}\left|\left(1-\lambda\frac{\sigma d}{\mathrm{j}\omega}\right)\right|\left|[\![p_h]\!]\left\langle\frac{1}{\rho}\frac{\partial p_h}{\partial n}\right\rangle_\gamma\right|\mathrm{d}S=2\sqrt{2}\int_{\Gamma^*}\frac{1}{\beta_h}|\lambda|\left|[\![p_h]\!]\left\langle\frac{1}{\rho}\frac{\partial p_h}{\partial n}\right\rangle_\gamma\right|\mathrm{d}S,\tag{A.10}$$

then using inequalities $2ab\leq 2a^2+b^2/2$, with $a=\sqrt{2}/\beta_h\left|\left\langle\frac{1}{\rho}\frac{\partial p_h}{\partial n}\right\rangle_\gamma\right|$, $b=\left|[\![p_h]\!]\right|$. The second term is written as:

$$\begin{aligned}
&2\sqrt{2}\int_{\Gamma^*}\frac{1}{\beta_h}|\lambda|\left|[\![p_h]\!]\left\langle\frac{1}{\rho}\frac{\partial p_h}{\partial n}\right\rangle_\gamma\right|\mathrm{d}S\\
&\leq 4\int_{\Gamma^*}\frac{1}{\beta_h^2}|\lambda|\left|\left\langle\frac{1}{\rho}\frac{\partial p_h}{\partial n}\right\rangle_\gamma\right|^2\mathrm{d}S+\frac{1}{2}\int_{\Gamma^*}|\lambda|\left|[\![p_h]\!]\right|^2\mathrm{d}S.
\end{aligned}\tag{A.11}$$

and with inequality eq. (30a):

$$\begin{aligned}
&4\int_{\Gamma^*}\frac{1}{\beta_h^2}|\lambda|\left|\left\langle\frac{1}{\rho}\frac{\partial p_h}{\partial n}\right\rangle_\gamma\right|^2\mathrm{d}S+\frac{1}{2}\int_{\Gamma^*}|\lambda|\left|[\![p_h]\!]\right|^2\mathrm{d}S\\
&\leq 4\int_{\Gamma^*}\frac{1}{\beta_h}\left|\left\langle\frac{1}{\rho}\frac{\partial p_h}{\partial n}\right\rangle_\gamma\right|^2\mathrm{d}S+\frac{1}{2}\int_{\Gamma^*}|\lambda|\left|[\![p_h]\!]\right|^2\mathrm{d}S.
\end{aligned}\tag{A.12}$$

Let us simplify the third term in eq. (A.9). The inequality eq. (30c) is first used, leading third term become as:

$$\begin{aligned}&\sqrt{2}\int_{\Gamma^*}\left|\frac{\sigma d}{\mathrm{j}\omega}\left(1-\lambda\frac{\sigma d}{\mathrm{j}\omega}\right)\right|\left|\left\langle\frac{1}{\rho}\frac{\partial p_h}{\partial n}\right\rangle_\gamma\right|^2\mathrm{d}S\\ \leq&\frac{2\sqrt{2}}{\beta_h}\int_{\Gamma^*}\left|\left\langle\frac{1}{\rho}\frac{\partial p_h}{\partial n}\right\rangle_\gamma\right|^2\mathrm{d}S\leq\frac{3}{\beta_h}\int_{\Gamma^*}\left|\left\langle\frac{1}{\rho}\frac{\partial p_h}{\partial n}\right\rangle_\gamma\right|^2\mathrm{d}S.\end{aligned}\tag{A.13}$$

Substituting inequalities eq. (A.12) and eq. (A.13) into eq. (A.9), we find that:

$$\begin{aligned}&\mathrm{Re}\left(a_\lambda(\bar{p}_h,p_h)\right)+\mathrm{Im}\left(a_\lambda(\bar{p}_h,p_h)\right)\\ \geq&|a_B(\bar{p}_h,p_h)|-\frac{7}{\beta_h}\int_{\Gamma^*}\left|\left\langle\frac{1}{\rho}\frac{\partial p_h}{\partial n}\right\rangle_\gamma\right|^2\mathrm{d}S+\int_{\Gamma^*}\left(\mathrm{Re}\left(\lambda\right)+\mathrm{Im}\left(\lambda\right)-\frac{1}{2}|\lambda|\right)|[\![p_h]\!]|^2\mathrm{d}S\\ =&|a_B(\bar{p}_h,p_h)|-\frac{8}{\beta_h}\int_{\Gamma^*}\left|\left\langle\frac{1}{\rho}\frac{\partial p_h}{\partial n}\right\rangle_\gamma\right|^2\mathrm{d}S+\frac{1}{\beta_h}\int_{\Gamma^*}\left|\left\langle\frac{1}{\rho}\frac{\partial p_h}{\partial n}\right\rangle_\gamma\right|^2\mathrm{d}S+\int_{\Gamma^*}\left(\mathrm{Re}\left(\lambda\right)+\mathrm{Im}\left(\lambda\right)-\frac{1}{2}|\lambda|\right)|[\![p_h]\!]|^2\mathrm{d}\end{aligned}\tag{A.14}$$

by the definition of $a_B$ with associated inequality for complex number $|w-z|\geq|w|-|z|$ and lemma 3.3, we are able to rewrite the eq. (A.9):

$$\begin{aligned}&\mathrm{Re}\left(a_\lambda(\bar{p}_h,p_h)\right)+\mathrm{Im}\left(a_\lambda(\bar{p}_h,p_h)\right)\geq\frac{1}{2}\sum_i^2\left|\frac{1}{\rho_i}\right|\int_{\Omega_i}|\boldsymbol{\nabla}p_h|^2\mathrm{d}\Omega-\sum_i^2\left|\frac{\omega^2}{K_i}\right|\int_{\Omega_i}|p_h|^2\mathrm{d}\Omega\\ +&\left(\frac{1}{2}-\frac{8}{\beta_h}C_I\right)\sum_i^2\int_{\Omega_i}\left|\frac{1}{\rho_i}\right|\left|\boldsymbol{\nabla}p_h\right|^2\mathrm{d}\Omega+\frac{1}{\beta_h}\int_{\Omega_i}\left|\left\langle\frac{1}{\rho}\frac{\partial p_h}{\partial n}\right\rangle_\gamma\right|^2\mathrm{d}\Omega+\int_{\Gamma^*}\left(\mathrm{Re}\left(\lambda\right)+\mathrm{Im}\left(\lambda\right)-\frac{1}{2}|\lambda|\right)|[\![p_h]\!]|^2\mathrm{d}S,\end{aligned}\tag{A.15}$$

to make term associated to $C_I$ be positive, the condition:

$$\begin{aligned}\left(\frac{1}{2}-\frac{8}{\beta_h}C_I\right)\geq0,\quad\text{that}\\ \beta_h\geq16C_I,\end{aligned}\tag{A.16}$$

and the last term in above equation replaced by the eq. (30d), we have finally:

$$\begin{aligned}\mathrm{Re}\left(a_\lambda(\bar{p}_h,p_h)\right)+\mathrm{Im}\left(a_\lambda(\bar{p}_h,p_h)\right)\geq&\frac{1}{2}\sum_i^2\left|\frac{1}{\rho_i}\right|\int_{\Omega_i}|\boldsymbol{\nabla}p_h|^2\mathrm{d}\Omega-\sum_i^2\left|\frac{\omega^2}{K_i}\right|\int_{\Omega_i}|p_h|^2\mathrm{d}\Omega\\ &+\frac{1}{\beta_h}\int_{\Omega_i}\left|\left\langle\frac{1}{\rho}\frac{\partial p_h}{\partial n}\right\rangle_\gamma\right|^2\mathrm{d}\Omega+\int_{\Gamma^*}\frac{1}{2}|\lambda||[\![p_h]\!]|^2\mathrm{d}S.\end{aligned}\tag{A.17}$$

Using that $2|z|\geq\mathrm{Re}\left(z\right)+\mathrm{Im}\left(z\right)$, and adding a multiple of $\|p\|$ with $C_k=2$: we finally

obtain:

$$
\begin{aligned}
2|a_\lambda(\bar{p}_h, p_h)| + 2\,\|p_h\|^2 \geq \frac{1}{2}\sum_i^2 \left|\frac{1}{\rho_i}\right| \int_{\Omega_i} |\boldsymbol{\nabla} p_h|^2 \mathrm{d}\Omega + \sum_i^2 \left|\frac{\omega^2}{K_i}\right| \int_{\Omega_i} |p_h|^2 \mathrm{d}\Omega \\
+ \frac{1}{\beta_h}\int_{\Omega_i} \left| \left\langle \frac{1}{\rho}\frac{\partial p_h}{\partial n} \right\rangle_\gamma \right|^2 \mathrm{d}\Omega + \int_{\Gamma^*} \frac{1}{2}|\lambda||[\![p]\!]|^2 \mathrm{d}S \\
\geq \frac{1}{2}|||p|||,
\end{aligned}
\tag{A.18}
$$

from which the Gårding equality holds for any $\beta_h \geq 16 C_I$ □

# B. Influence of localization of the interface inside cut elements

This appendix provides complementary results on the influence of the interface position with respect to cut-elements as elaborated in section 4.1.2. The experiment is conducted within 1D elements ($h \simeq 1$cm) and approximation order p = 3. The material contrast is chosen relatively small ($|\rho_a| = 1.213$ and $|\rho_f| = 2.108$) to focus on the influence of the interface localization.The interface is moved from the middle of the element to extremely close to the boundary. We plot the constant $C_I$ calculated from classical and robust strategies as function of the relative interface position inside the element, as shown in fig. B.1.

It is noticeable that constants $C_I$ obtained by the robust strategy are virtually not impacted by the interface position with respect to the cut-element, while an large increase is observed if it is evaluated using the classical strategy, especially when interface is close to the element boundary. This result is consistent with observations with 2D unstructured meshes and analysis in section 3.3, demonstrating the advantage of using the robust strategy to evaluate the stability parameter.

# C. Equivalent fluid model for dissipative materials

Table C.1: Porous materials parameters for bulk part

| Parameters | Plastic foam | classical foam | XFM |
|---|---|---|---|
| Porosity $\phi\,(-)$ | 0.97 | 0.98 | 0.98 |
| static flow resistivity $\sigma\,(\mathrm{N\,m^{-4}s})$ | $57 \times 10^3$ | $15.5 \times 10^3$ | $13.5 \times 10^3$ |
| Tortuosity $\alpha\,(-)$ | 1.54 | 1.01 | 1.7 |
| thermal characteristic length $\Lambda'\,(\mathrm{m})$ | $73.8 \times 10^{-6}$ | $250 \times 10^{-6}$ | $160 \times 10^{-6}$ |
| Viscous characteristic length $\Lambda\,(\mathrm{m})$ | $24.6 \times 10^{-6}$ | $100 \times 10^{-6}$ | $80 \times 10^{-6}$ |

We present one of equivalent fluid models, JCA model [3, 4] that is used in this paper for modelling acoustic behaviour of porous materials. The complex-valued properties can be calculated with the measured material parameters given in table C.1. The analytical

expression of the effective density $\rho_{\mathrm{eq}}$ reads as:

$$\rho_{\mathrm{eq}} = \frac{\rho_{\mathrm{a}}\alpha_\infty}{\phi}\left[1 + \frac{\sigma\phi}{\mathrm{j}\omega\rho_{\mathrm{a}}\alpha_\infty}\sqrt{1 + \frac{4\mathrm{j}\omega\alpha_\infty^2\mu\rho_{\mathrm{a}}}{\sigma^2\Lambda^2\phi^2}}\right], \tag{C.1}$$

and the effective compressibility $K_{\mathrm{eq}}$:

$$K_{\mathrm{eq}} = \frac{\gamma P_0}{\phi}\left[\gamma - (\gamma-1)\left(1 + \frac{8\mu}{\mathrm{j}\omega\Lambda'^2\mathrm{Pr}\rho_a}\sqrt{1 + \frac{\mathrm{j}\omega\rho_a\mathrm{Pr}\Lambda'^2}{16\mu}}\right)\right]^{-1}, \tag{C.2}$$

where $\rho_a$, $\eta_a$ are the density of air and dynamic viscosity of the fluid. $\gamma$ represents the ratio of specific heats of air, $P_0$ is the referred ambient pressure, Pr denotes the Prandtl number. More detail can be referred in textbook [45].

## D. Analytical solutions

We provide the analytical solutions for two plane wave benchmarks. The exact solution of oblique plane wave propagation in a two-media infinite plane section 4.1.2 is given as:

$$p_a = \exp(-\mathrm{j}k_{\mathrm{a}x}x - \mathrm{j}k_{\mathrm{a}y}y) + R\exp(\mathrm{j}k_{\mathrm{a}x}x - \mathrm{j}k_{\mathrm{a}y}y), \tag{D.1a}$$

$$p_f = T\exp(-\mathrm{j}k_{\mathrm{f}x}x - \mathrm{j}k_{\mathrm{f}y}y), \tag{D.1b}$$

with reflection and transmission coefficient $R$, $T$:

$$T = 2/(1 + \rho_a k_{\mathrm{f}x}/(\rho_{\mathrm{f}}k_{\mathrm{a}x}) + \sigma d k_{\mathrm{f}x}/(\rho_f\omega)), \tag{D.2a}$$

$$R = 1 - \rho_{\mathrm{a}}k_{\mathrm{f}x}/(\rho_{\mathrm{f}}k_{\mathrm{a}x})T, \tag{D.2b}$$

where $k_{\mathrm{a}x}$, $k_{\mathrm{a}y}$, $k_{\mathrm{f}x}$ and $k_{\mathrm{f}y}$ correspond to the directional components of wave number for air and foam. $\rho_a$ and $\rho_f$ are the effective density of air and foam.

Regarding the cylinder scattering problem as in fig. 14, the pressure field under unit amplitude incident is expressed with Hankel $\mathrm{H}_m$ and Bessel function $\mathrm{J}_m$ in polar coordinate as:

$$p_a = \rho_{\mathrm{a}}\omega^2\left(\mathrm{J}_0(k_{\mathrm{a}}r) + 2\sum_{m=1}^{\infty}(-\mathrm{j})^m\mathrm{J}_m(k_{\mathrm{a}}r)\cos(m\theta) + \sum_{m=0}^{\infty}R_m\mathrm{H}_m(k_{\mathrm{a}}r)\cos(m\theta)\right) \tag{D.3a}$$

$$p_f = \rho_{\mathrm{f}}\omega^2\sum_{m=0}^{\infty}T_m(-\mathrm{j})^m\mathrm{J}_m(k_{\mathrm{f}}r)\cos(m\theta), \tag{D.3b}$$

applying the interface conditions at $r = R$ to obtain coefficients $R_m$ and $T_m$, Thus, we

have a linear system of $2 \times 2$ to solve. The left-hand side matrix of the system are:

$$M_{1,1} = \rho_{\mathrm{a}} \mathrm{H}_m(k_{\mathrm{a}} R) \tag{D.4a}$$

$$M_{1,2} = -\rho_{\mathrm{f}} \mathrm{J}_m(k_{\mathrm{f}} R) - \frac{\sigma d}{\mathrm{j}\omega} k_{\mathrm{f}} \mathrm{J}'_m(k_{\mathrm{f}} R) \tag{D.4b}$$

$$M_{2,1} = k_{\mathrm{a}} \mathrm{H}'_m(k_{\mathrm{a}} R) \tag{D.4c}$$

$$M_{2,2} = -k_{\mathrm{f}} \mathrm{J}'_m(k_{\mathrm{f}} R), \tag{D.4d}$$

and with right-hand side vector:

$$b_1 = -2\rho_{\mathrm{a}} (-\mathrm{j})^m \mathrm{J}_m(k_a R), \tag{D.5a}$$

$$b_2 = -2k_a (-\mathrm{j})^m \mathrm{J}'_m(k_a R), \tag{D.5b}$$

where $\mathrm{J}'_m$ and $\mathrm{H}'_m$ are the first order derivative of Bessel and Hankel functions, respectively.

## References


[1] M. A. Biot. Theory of Propagation of Elastic Waves in a Fluid-Saturated Porous Solid. I. Low-Frequency Range. The Journal of the Acoustical Society of America, 28(2):168–178, March 1956.

[2] Maurice A Biot. Mechanics of deformation and acoustic propagation in porous media. page 19, 1962.

[3] David Linton Johnson, Joel Koplik, and Roger Dashen. Theory of dynamic permeability and tortuosity in fluid-saturated porous media. Journal of Fluid Mechanics, 176:379–402, March 1987.

[4] Yvan Champoux and Jean-F. Allard. Dynamic tortuosity and bulk modulus in air-saturated porous media. Journal of Applied Physics, 70(4):1975–1979, August 1991.

[5] Srinivas Katragadda, Heng-Yi Lai, and J. Stuart Bolton. A model for sound absorption by and sound transmission through limp fibrous layers. The Journal of the Acoustical Society of America, 98(5):2977–2977, November 1995.

[6] Peter Bövik. On the modelling of thin interface layers in elastic scattering problems. The Quarterly Journal of Mechanics and Applied Mathematics, 47(1):17–42, February 1994.

[7] Allan Pierce. Acoustics: An Introduction to Its Physical Principles and Applications, volume 34. June 1989.

[8] Arnaud Deraemaeker, Ivo Babus, and Philippe Bouillard. Dispersion and pollution of the FEM solution for the Helmholtz equation in one, two and three dimensions. page 29, 1999.

[9] F. Ihlenburg and I. Babuška. Finite element solution of the Helmholtz equation with high wave number Part I: The h-version of the FEM. Computers & Mathematics with Applications, 30(9):9–37, November 1995.

[10] Frank Ihlenburg and Ivo Babuska. Finite Element Solution of the Helmholtz Equation with High Wave Number Part II: The h-p Version of the FEM. SIAM Journal on Numerical Analysis, 34(1):315–358, February 1997.

[11] Hadrien Bériot, Gwénaël Gabard, and Emmanuel Perrey-Debain. Analysis of high-order finite elements for convected wave propagation: High-order finite elements for convected acoustics. International Journal for Numerical Methods in Engineering, 96(11):665–688, December 2013.

[12] Hadrien Bériot, Albert Prinn, and Gwénaël Gabard. Efficient implementation of high-order finite elements for Helmholtz problems. International Journal for Numerical Methods in Engineering, 106(3):213–240, April 2016.

[13] J.-D. Chazot, B. Nennig, and E. Perrey-Debain. Performances of the Partition of Unity Finite Element Method for the analysis of two-dimensional interior sound fields with absorbing materials. Journal of Sound and Vibration, 332(8):1918–1929, April 2013.

[14] Nicolas Moës, John Dolbow, and Ted Belytschko. A finite element method for crack growth without remeshing. International Journal for Numerical Methods in Engineering, 46(1):131–150, 1999.

[15] Ivo Babuška, Uday Banerjee, and John E. Osborn. Generalized finite element methods — main ideas, results and perspective. International Journal of Computational Methods, 01(01):67–103, June 2004.

[16] N Sukumar, D L Chopp, and N Mo. Modeling holes and inclusions by level sets in the extended finite-element method. Comput. Methods Appl. Mech. Engrg., page 18, 2001.

[17] N. Moës, M. Cloirec, P. Cartraud, and J.-F. Remacle. A computational approach to handle complex microstructure geometries. Computer Methods in Applied Mechanics and Engineering, 192(28-30):3163–3177, July 2003.

[18] Axel Gerstenberger and Wolfgang A. Wall. An eXtended Finite Element Method/Lagrange multiplier based approach for fluid–structure interaction. Computer Methods in Applied Mechanics and Engineering, 197(19):1699–1714, March 2008.

[19] Thomas-Peter Fries and Ted Belytschko. The extended/generalized finite element method: An overview of the method and its applications. International Journal for Numerical Methods in Engineering, 84(3):253–304, October 2010.

[20] Simon-Nicolas Roth, Pierre Léger, and Azzeddine Soulaïmani. Strongly coupled XFEM formulation for non-planar three-dimensional simulation of hydraulic fracturing with emphasis on concrete dams. Computer Methods in Applied Mechanics and Engineering, 363:112899, May 2020.

[21] Anita Hansbo and Peter Hansbo. An unfitted finite element method, based on Nitsche's method, for elliptic interface problems. Computer Methods in Applied Mechanics and Engineering, 191(47-48):5537–5552, November 2002.

[22] Jeong-Hoon Song, Pedro M. A. Areias, and Ted Belytschko. A method for dynamic crack and shear band propagation with phantom nodes. International Journal for Numerical Methods in Engineering, 67(6):868–893, 2006.

[23] Zilong Zou, Wilkins Aquino, and Isaac Harari. Nitsche's method for Helmholtz problems with embedded interfaces. International Journal for Numerical Methods in Engineering, 110(7):618–636, May 2017.

[24] Anita Hansbo, Peter Hansbo, and Mats G. Larson. A finite element method on composite grids based on Nitsche's method. ESAIM: Mathematical Modelling and Numerical Analysis, 37(3):495–514, May 2003.

[25] P. Hansbo and J. Hermansson. Nitsche's method for coupling non-matching meshes in fluid-structure vibration problems. Computational Mechanics, 32(1-2):134–139, September 2003.

[26] Peter Hansbo, Mats G. Larson, and Sara Zahedi. A cut finite element method for a Stokes interface problem. Applied Numerical Mathematics, 85:90–114, November 2014.

[27] A. Johansson, M. Garzon, and J. A. Sethian. A three-dimensional coupled Nitsche and level set method for electrohydrodynamic potential flows in moving domains. Journal of Computational Physics, 309:88–111, March 2016.

[28] C. Ager, B. Schott, M. Winter, and W.A. Wall. A Nitsche-based cut finite element method for the coupling of incompressible fluid flow with poroelasticity. Computer Methods in Applied Mechanics and Engineering, 351:253–280, July 2019.

[29] Erik Burman, Susanne Claus, Peter Hansbo, Mats G. Larson, and André Massing. CutFEM: Discretizing geometry and partial differential equations. International Journal for Numerical Methods in Engineering, 104(7):472–501, 2015.

[30] Pedro M.A. Areias and Ted Belytschko. A comment on the article "A finite element method for simulation of strong and weak discontinuities in solid mechanics" by A. Hansbo and P. Hansbo [Comput. Methods Appl. Mech. Engrg. 193 (2004) 3523–3540]. Computer Methods in Applied Mechanics and Engineering, 195(9-12):1275–1276, February 2006.

[31] I. Babuska. The Finite Element Method with Penalty. 1973.

[32] D. S. Malkus. Incompressible Finite Elements: The LBB Condition and the Discrete Eigenstructure. In W. Wunderlich, E. Stein, and K.-J. Bathe, editors, Nonlinear Finite Element Analysis in Structural Mechanics, pages 696–711, Berlin, Heidelberg, 1981. Springer.

[33] J. Nitsche. über ein Variationsprinzip zur Lösung von Dirichlet-Problemen bei Verwendung von Teilräumen, die keinen Randbedingungen unterworfen sind. 1971.

[34] Martin Hautefeuille, Chandrasekhar Annavarapu, and John E. Dolbow. Robust imposition of Dirichlet boundary conditions on embedded surfaces. International Journal for Numerical Methods in Engineering, 90(1):40–64, 2012.

[35] Roland Becker, Erik Burman, and Peter Hansbo. A hierarchical NXFEM for fictitious domain simulations. page 11, 2010.

[36] Erik Burman and Peter Hansbo. Fictitious domain finite element methods using cut elements: II. A stabilized Nitsche method. Applied Numerical Mathematics, 62(4):328–341, April 2012.

[37] John Dolbow and Isaac Harari. An efficient finite element method for embedded interface problems. International Journal for Numerical Methods in Engineering, 78(2):229–252, April 2009.

[38] Chandrasekhar Annavarapu, Martin Hautefeuille, and John E. Dolbow. A Nitsche stabilized finite element method for frictional sliding on embedded interfaces. Part II: Intersecting interfaces. Computer Methods in Applied Mechanics and Engineering, 267:318–341, December 2013.

[39] Erik Burman. Ghost penalty. Comptes Rendus Mathematique, 348(21-22):1217–1220, November 2010.

[40] Frédéric Alauzet, Benoit Fabrèges, Miguel A. Fernández, and Mikel Landajuela. Nitsche-XFEM for the coupling of an incompressible fluid with immersed thin-walled structures. Computer Methods in Applied Mechanics and Engineering, 301:300–335, April 2016.

[41] Chandrasekhar Annavarapu, Martin Hautefeuille, and John E. Dolbow. A robust Nitsche's formulation for interface problems. Computer Methods in Applied Mechanics and Engineering, 225–228:44–54, June 2012.

[42] Wen Jiang, Chandrasekhar Annavarapu, John E. Dolbow, and Isaac Harari. A robust Nitsche's formulation for interface problems with spline-based finite elements: A robust Nitsche's formulation for interface problems with spline-based finite elements. International Journal for Numerical Methods in Engineering, 104(7):676–696, November 2015.

[43] Wen Jiang, Yingjie Liu, and Chandrasekhar Annavarapu. A weighted Nitsche's method for interface problems with higher-order simplex elements. Computational Mechanics, January 2022.

[44] Esubalewe Lakie Yedeg, Eddie Wadbro, Peter Hansbo, Mats G. Larson, and Martin Berggren. A Nitsche-type method for Helmholtz equation with an embedded acoustically permeable interface. Computer Methods in Applied Mechanics and Engineering, 304:479–500, June 2016.

[45] J.-F. Allard and Noureddine Atalla. Propagation of Sound in Porous Media: Modelling Sound Absorbing Materials. Wiley, Hoboken, N.J, 2nd ed edition, 2009.

[46] Frank Ihlenburg. Finite Element Analysis of Acoustic Scattering. 1998.

[47] Anita Hansbo and Peter Hansbo. A finite element method for the simulation of strong and weak discontinuities in solid mechanics. Computer Methods in Applied Mechanics and Engineering, 193(33-35):3523–3540, August 2004.

[48] Q.-Z. Zhu, S.-T. Gu, J. Yvonnet, J.-F. Shao, and Q.-C. He. Three-dimensional numerical modelling by XFEM of spring-layer imperfect curved interfaces with applications to linearly elastic composite materials. International Journal for Numerical Methods in Engineering, 88(4):307–328, October 2011.

[49] Stanley Osher and James A Sethian. Fronts propagating with curvature-dependent speed: Algorithms based on Hamilton-Jacobi formulations. Journal of Computational Physics, 79(1):12–49, November 1988.

[50] G. Legrain, N. Chevaugeon, and K. Dréau. High order X-FEM and levelsets for complex microstructures: Uncoupling geometry and approximation. Computer Methods in Applied Mechanics and Engineering, 241–244:172–189, October 2012.

[51] Goangseup Zi and Ted Belytschko. New crack-tip elements for XFEM and applications to cohesive cracks. International Journal for Numerical Methods in Engineering, 57(15):2221–2240, August 2003.

[52] Chandrasekhar Annavarapu, Martin Hautefeuille, and John E. Dolbow. A Nitsche stabilized finite element method for frictional sliding on embedded interfaces. Part I: Single interface. Computer Methods in Applied Mechanics and Engineering, 268:417–436, January 2014.

[53] T. Menouillard, J. Réthoré, N. Moës, A. Combescure, and H. Bung. Mass lumping strategies for X-FEM explicit dynamics: Application to crack propagation: MASS LUMPING STRATEGIES FOR X-FEM EXPLICIT DYNAMICS. International Journal for Numerical Methods in Engineering, 74(3):447–474, April 2008.

[54] Anand Embar, John Dolbow, and Isaac Harari. Imposing Dirichlet boundary conditions with Nitsche's method and spline-based finite elements. International Journal for Numerical Methods in Engineering, pages n/a–n/a, 2010.

[55] Shaoqi Wu, Olivier Dazel, Gwénaël Gabard, and Grégory Legrain. High-order X-FEM for the simulation of sound absorbing poro-elastic materials with coupling interfaces. Journal of Sound and Vibration, 510:116262, October 2021.

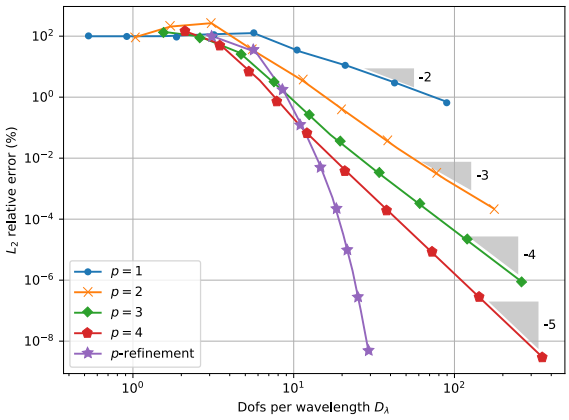


(a)

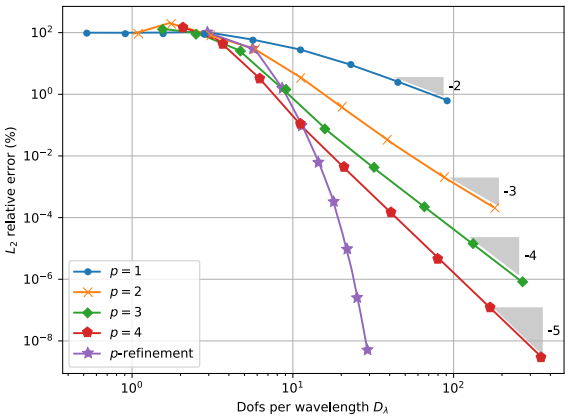


(b)

Figure 7: $L^2$ convergence of the Nitsche-type formulation for perfect and imperfect interface ($\sigma d = 775\ \mathrm{N\,s\,m^{-3}}$) conditions.

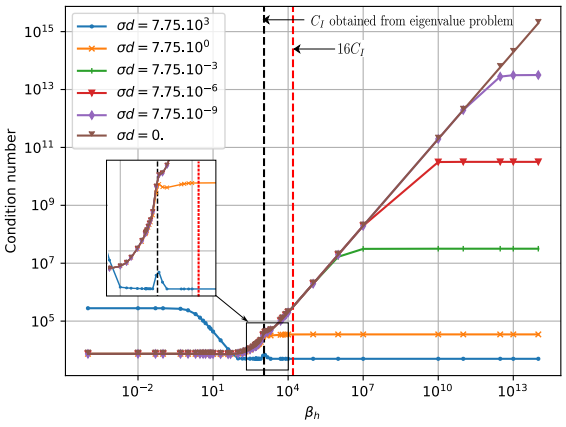


Figure 8: Sensitivity of the conditioning number w.r.t the stability parameter $\beta_h$ (p = 3) for different film parameters $\sigma d$.

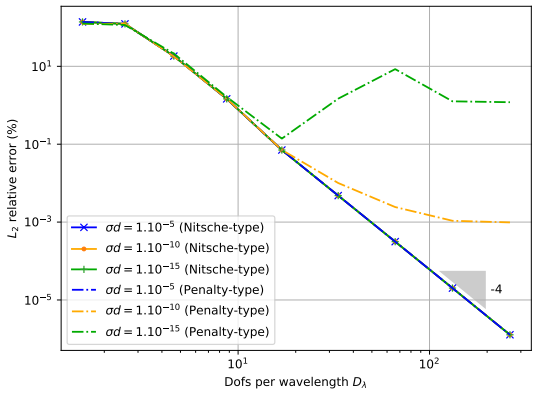


(a)

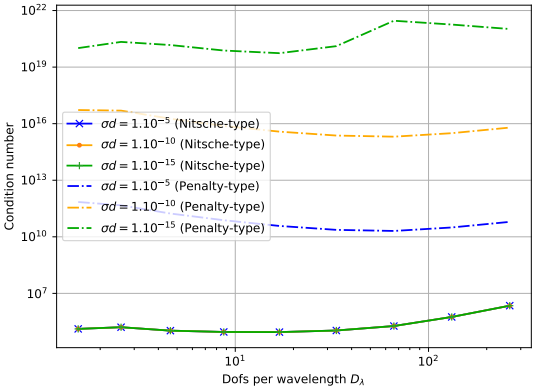


(b)

Figure 9: (a) $L^2$ convergence and (b) conditioning of the *Nitsche-type* and *penalty-type* formulations for different $\sigma d$ (polynomial order p = 3).

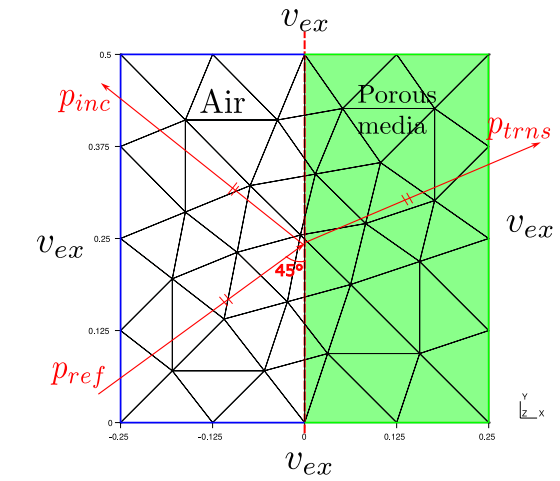


(a)

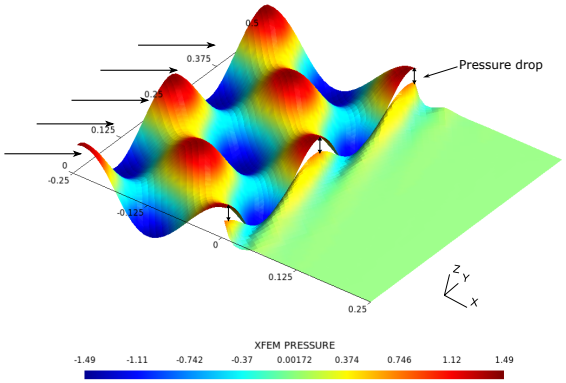


(b)

Figure 10: Oblique incident wave: (a) Problem set-up and (b) Example of solution obtained by the proposed approach (real part, in Pa). One can observe a pressure drop and a change in the direction of the wave propagation across the interface.

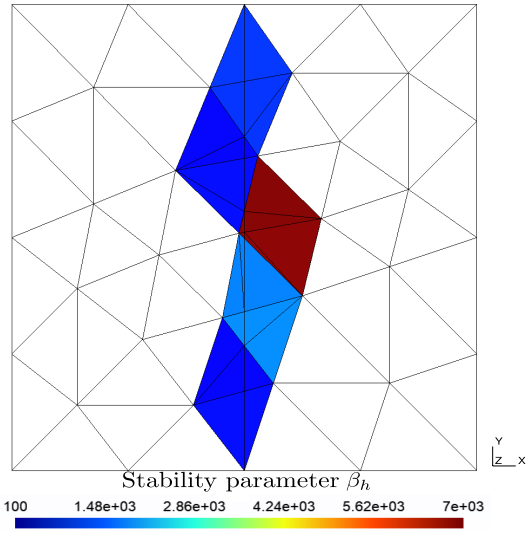


(a)

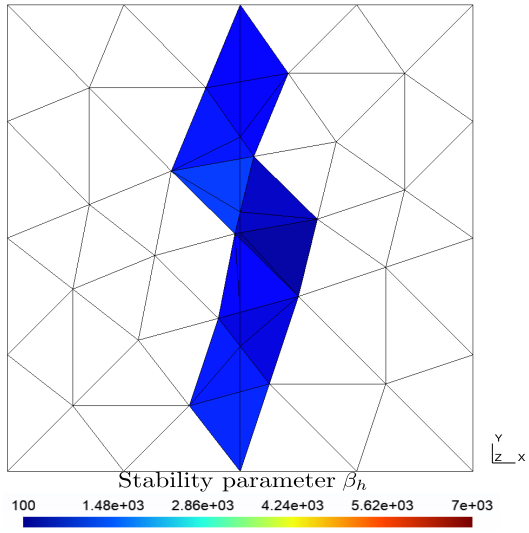


(b)

Figure 11: Evaluation of stability parameter $\beta_h$ by (a) classical strategy ($\gamma = 0.5$) and (b) robust strategy ($\gamma$-Nitsche).

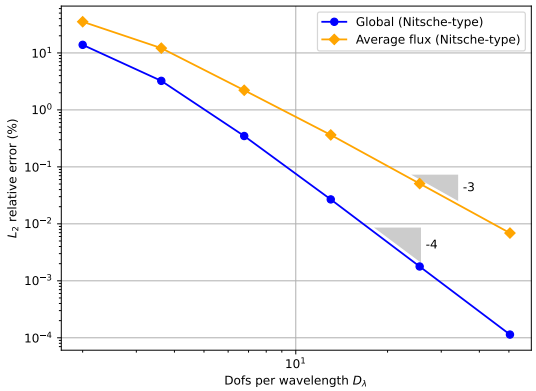


(a)

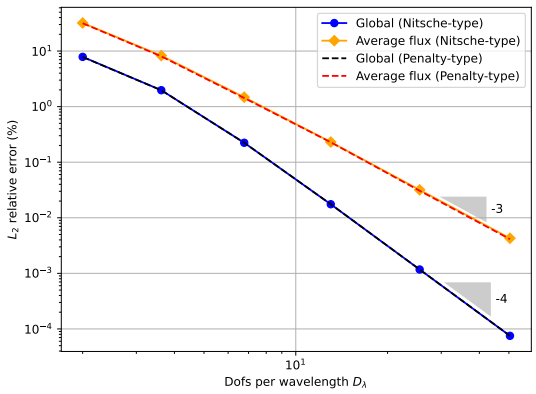


(b)

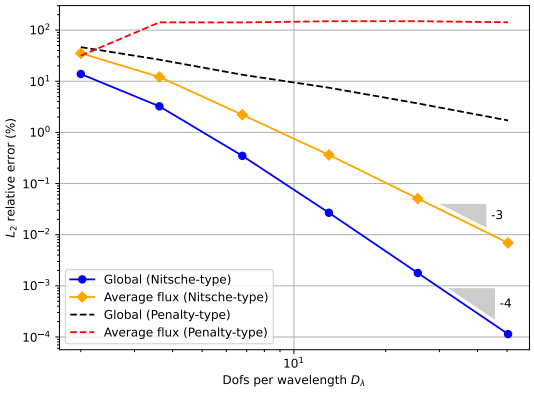


(c)

Figure 12: Global error in the bulk and average interfacial flux for (a) perfect interface; (b) imperfect interface ($\sigma d = 775\mathrm{N\,s\,m^{-3}}$); (c) near-perfect interface ($\sigma d = 1.10^{-15}\mathrm{N\,s\,m^{-3}}$).

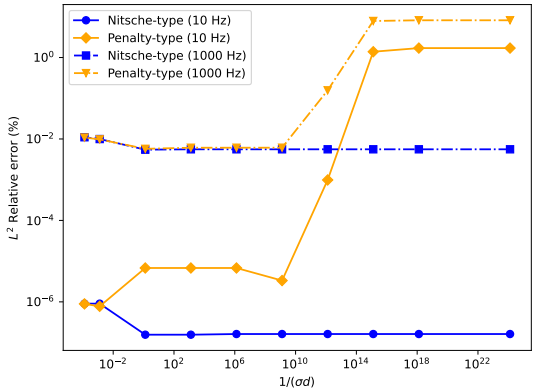


(a)

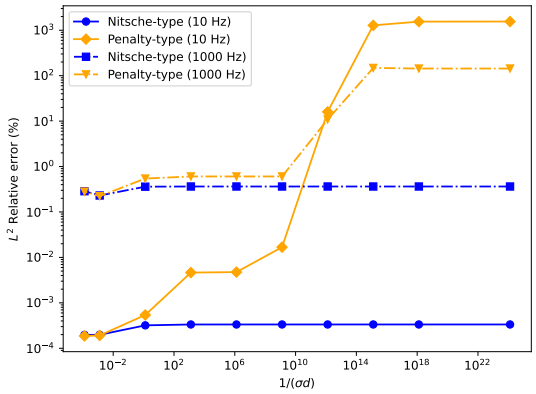


(b)

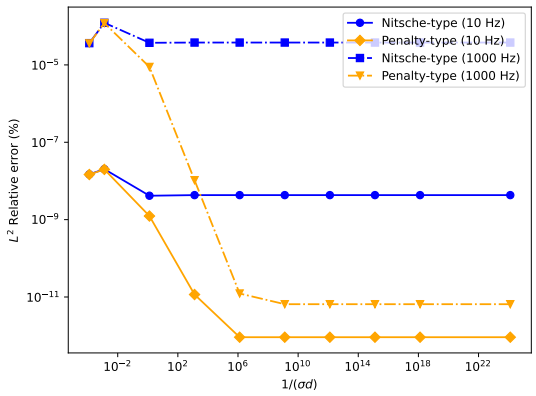


(c)

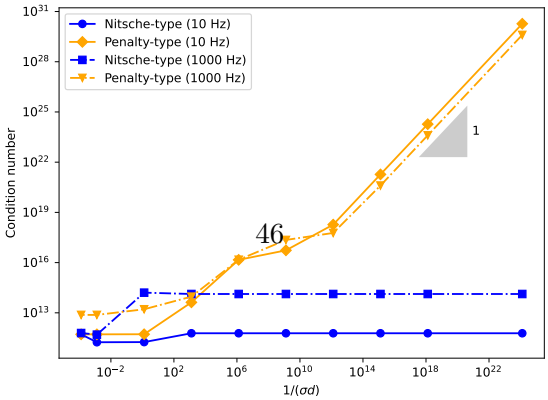


(d)

Figure 13: (a) Relative error on the pressure; (b) relative error on the interfacial flux (c) absolute jump error; (d) condition number of global matrix with respect to

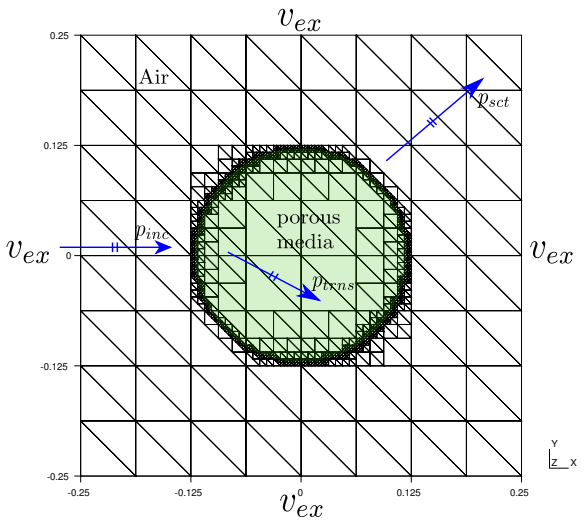


(a)

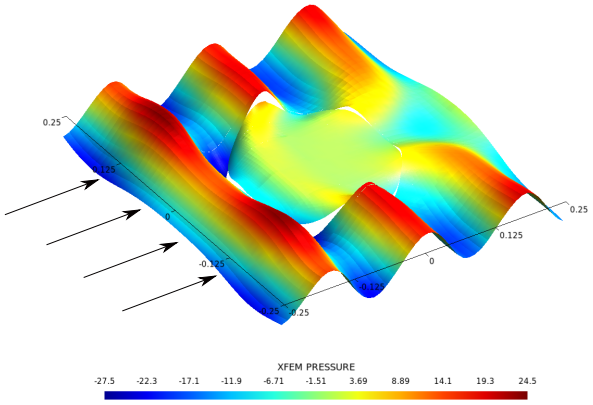


(b)

Figure 14: (a) Problem setup and mesh with refined geometric elements for a curved interface; (b) Example of real part the pressure (in Pa) under excitation of $2,000$ Hz ($p = 4$).

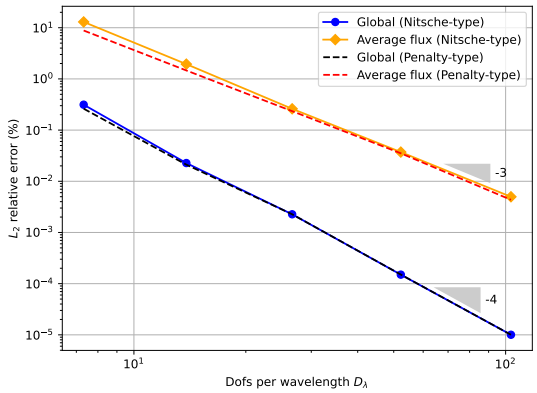


(a)

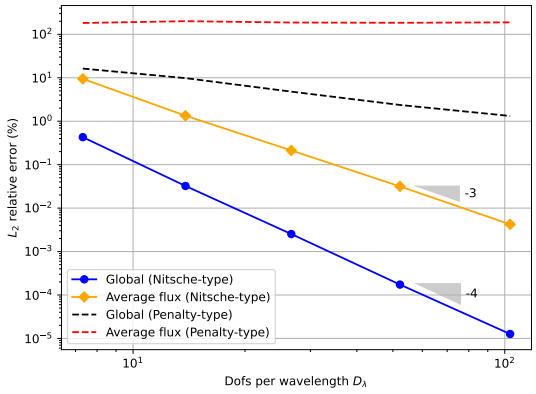


(b)

Figure 15: Global error in the bulk and average interfacial flux for (a) imperfect interface ($\sigma d = 775\mathrm{N\,s\,m^{-3}}$); (b) near-perfect interface ($\sigma d = 1.10^{-15}\mathrm{N\,s\,m^{-3}}$).

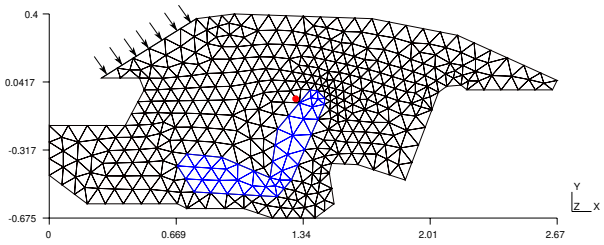


(a)

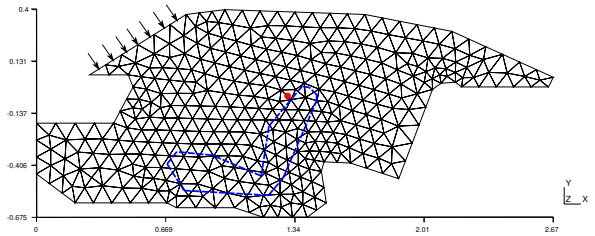


(b)

Figure 16: Problem setup and corresponding meshes (a) using interface-fitted FEM and (b) embedded interface with X-FEM.

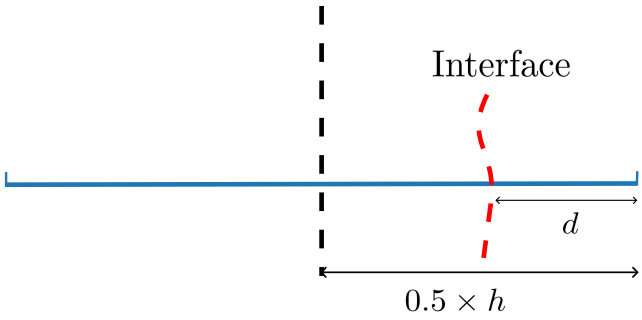


(a)

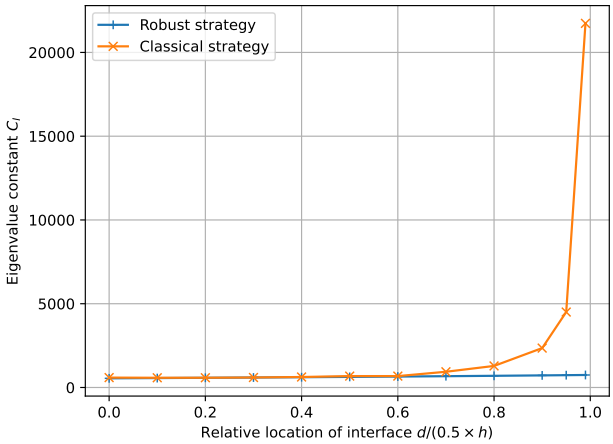


(b)

Figure B.1: Influence of interface localization inside elements using two evaluation strategies for proposed Nitsche formulation